Design Study of a Permanent Magnet Assisted Synchronous Reluctance Generator for Wind Turbines

Master Thesis

WPS4/950

Carlos Enrique Imbaquingo Muñoz

Aalborg University
Department of Energy Technology
Pontoppidanstræde 111
DK-9220 Aalborg

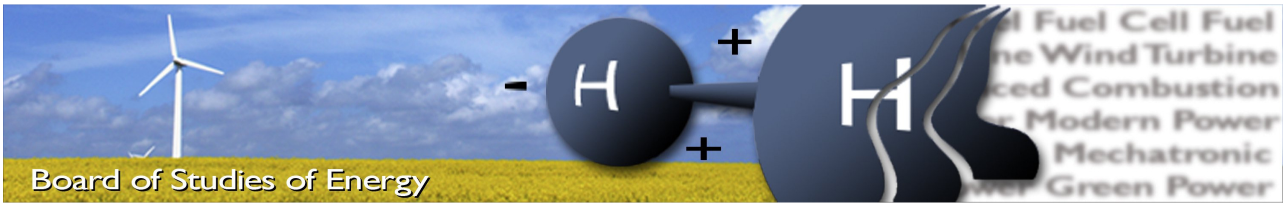

Title: Design Study of a Permanent Magnet Assisted Synchronous Reluctance Generator for Wind Turbines
Semester: 10
Semester theme: Scientific
Project period: 04.09.17 to 01.06.18
ECTS: 50
Supervisor: Kaiyuan Lu
Project group: WPS4-950

Carlos Enrique Imbaquingo Muñoz

SYNOPSIS:

In this project, a study design of a FMaSynRM is realized, where a finite element method based software (OperaFEA) is employed. First, the simulation analysis of an existing 13-kW SynRM is done, whose electromagnetic parameters are calculated and compared with experimental ones. Then, the design of a 4-pole 5-MW FMaSynRG is performed by taking into account some physical rotor characteristics, such as asymmetric flux barriers and magnet coverage. These outcomes are contrasted with a 8-pole 5-MW IPMSG attaining similar results with lower active material weight. Finally, a wind power generation system is modelled with a FMaSynRG, where the MTPA strategy is employed.

Pages, total: 90
Appendix: 9
Supplements: 11

By accepting the request from the fellow student who uploads the study group's project report in Digital Exam System, you confirm that all group members have participated in the project work, and thereby all members are collectively liable for the contents of the report. Furthermore, all group members confirm that the report does not include plagiarism.

Contents

Preface

This project is submitted to Aalborg University, School of Engineering and Science, Department of Energy Technology, Denmark in partial fulfillment of the requirements for the degree of Master in Wind Power Systems.
The main purpose of this project is to explain the necessary concepts to design an electrical machine. Additionally, a wind power generation system is detailed and the required controllers are designed.

Aalborg University, May 31, 2018

Carlos Enrique Imbaquingo Muñoz
<cimbaq16@student.aau.dk>

Summary

A Synchronous Reluctance Machine (SynRM) has become an interesting competitor to Permanent Magnet Synchronous Machines (PMSM's) due to the lack of rare-earth permanent magnets, and to Induction Machines (IM's) because of simple structure and lower cost. Furthermore, when ferrite magnets are placed into the flux barriers a high performance is achieved, resulting in a Ferrite Magnet-assisted Synchronous Reluctance Machine (FMaSynRM). Subsequently, power factor is improved and torque ripple is reduced. Moreover, the cost of the machine decreases since lower rotor core material is needed, and ferrite magnets are by far cheaper than rare-earth permanent magnets. Nonetheless, the manufacturing rotor process comprises a magnetization step, where a Halbach ring is essential. The problem lies on the size of the Halbach ring, since the rotor must be placed in its center.

The main task of this project is to realize a study design of a Ferrite Magnet-assisted Reluctance Generator (FmaSynRG) for wind energy applications. The project starts with a simulation of a Synchronous Reluctance Motor in a finite element method based software (OperaFEA). This task aims to define the steps to find the electromagnetic parameters of the electrical machine, and subsequently to contrast the outcomes with the measured parameters of an existing machine to validate the procedure. After that, a couple of 5-MW generators for wind energy applications are designed by considering previous researches. An important approach is taken in the flux barrier asymmetric shape, as well as in the magnet coverage. The results will show that only one of these approaches can be accomplished. Finally, a wind turbine power generation system is performed, where the FMaSynRG is represented by its mathematical model. To establish the closed loop control system, two PI controllers are designed, whose current references are settled by the Maximum Torque Per Ampere (MTPA) strategy. Furthermore, to make easier the design, the controller implements a decoupling loop of the back-EMF, so the plant becomes a first order system. And also, the computational and PWM delays are considered in the case that this model is extended to a complete power-flowing-to-grid circuit.

Glossary of Terms

abc	three-phase frame
A_c	cross-sectional core area
$\overrightarrow{A}$	vector magnetic potential
A_{xz}	xz-plane area
b_1	inner slot base
b_2	outer slot base
b_d	tooth width
$\overrightarrow{B}$	magnetic flux density
$\hat{B}_\delta$	air-gap magnetic flux density
$\hat{B}_d$	permitted magnetic flux density
back-EMF	back electromotive force
$cos(\phi)$	power factor
$dq0$	rotating frame
$\overrightarrow{D}$	electric flux density
D_c	diameter of a circle whose ratio ends in the middle of a slot
D_s	inner stator diameter
DFIG	double fed induction generator
$\overrightarrow{E}$	electric field
e	electromotive force
e_d	electromotive force in d-axis
e_m	motion electromotive force
e_q	electromotive force in q-axis
e_t	transfomer electromotive force
e_ϕ	phase electromotive force
EMF	electromotive force
f	function
f_1	fundamental frequency
f_s	sampling frequency
$\overrightarrow{F}$	force
$\mathcal{F}$	magnetomotive force
FMaSynRG	ferrite magnet-assisted synchronous reluctance generator
FMaSynRM	ferrite magnet-assisted synchronous reluctance machine (or motor)
g	air gap
G_c	controller transfer function
G_d	delay transfer functio
G_p	plant transfer functio
GM	gain margin
$\overrightarrow{H}$	magnetic strength

i	electric current
i_s	current space vector
i_d	d-axis current
i_d^*	d-axis reference current
i_q	q-axis current
i_q^*	q-axis reference current
I	continuous electric current
IM	induction machine
IPMSG	internal-mounted permanent magnet synchronous machine
J	inertia
$\overrightarrow{J}$	current density
k_f	fill factor
k_{fe}	space factor of iron
k_{sat}	saturation factor
k_{w1}	fundamental winding factor
K_i	integral constant
K_p	proportional constant
$\overrightarrow{K}$	linear current density
ℓ	machine length
ℓ'	equivalent length
ℓ_c	conductor length
ℓ_k	loop length
l_c	core length
L	inductance
L_d	d-axis inductance
L_{ls}	leakage inductance
L_{md}	d-axis main inductance
L_{mq}	q-axis main inductance
L_q	q-axis inductance
L_s	stator inductance
L_x	x-axis length
L_z	z-axis length
m	number of phases
M	mutual inductance
MMF	magnetomotive force
MTPA	maximum torque per ampere
$\overrightarrow{n}$	normal vector
N	number of turns
N	north pole
N_Φ	number of conductor/phase/pole
$n_v b_v$	number of ventilation ducts
n_c	number of conductor in one slot
$\mathfrak{p}$	number of pole-pair
P_{cu}	copper losses
P_{fe}	iron losses
P_{in}	input power
P_{out}	output power

PMSG	permanent magnet synchronous generator
PMSM	permanent magnet synchronous motor
PWM	pulse width modulation
q	electric charge
q	number of slots/pole/phase
$\mathcal{Q}$	total number of slots
r_{branch}	resistance in one branch
r_r	outer rotor ratio
r_s	phase stator resistance
reg_n	nth air-gap region
R	distance
R_1	first rotor structure
R_2	second rotor structure
R_s	stator resistance matrix
RHP	right hand plane
$\mathcal{R}$	reluctance
S	south pole
S_c	cross-sectional conductor area
S_{slot}	cross-sectional slot area
SCIG	squirrel cage induction generator
SG	synchronous generator
SynRM	synchronous reluctance generator
T_s	sampling period
$\overrightarrow{T}$	torque vector
$\overrightarrow{v}$	velocity
v_d	d-axis voltage
v_q	q-axis voltage
V_m	scalar magnetic potential
$y_{\mathcal{Q}}$	number of slots/pole
α_i	average coefficient of flux density
ϵ_o	permittivity in free space
ϵ_r	dielectric constant
η	efficiency
θ	angle
θ_r	electric position angle
λ	induced flux
λ_d	d-axis flux
λ_q	q-axis flux
λ_{mpm}	peak magnitude of permanent magnet
μ_o	permeability in free space
μ_r	permeability of the medium
ρ	resistivity
ρ_v	charge density
σ_F	magnetic stress
σ_{F_n}	stress normal component
$\sigma_{F_{tan}}$	stress tangential component
τ_i	integral time
τ_p	pole pitch
$\tau_{p,c}$	circle arc covered by conductor
τ_u	slot pitch

ϕ	induced flux in one loop
ϕ_m	phase margin
φ	magnetic flux through the core
ω_c	crossover frequency
ω_m	mechanical angular speed
ω_r	electrical angular speed

Chapter 1

Introduction

Over the last decades, wind energy has been one of the fastest growing renewable energy sources. By the end of 2016, over 90 countries had seen commercial wind activity, and 29 countries had more than 1 GW in operation [1]. The energy conversion from mechanical to electric has been done by different generator types. These include the Squirrel Cage Induction Generator (SCIG), Doubly Fed Induction Generator (DFIG), and Synchronous Generator (SG) with wound rotor or permanent magnets [2]. Permanent Magnet Synchronous Generators (PMSG's) have higher efficiency and power density as compared to the other generator types. However, the use of rare-earth permanent magnets has increased manufacturing cost, leading to finding an alternative generator option.

Since the first publication of a Synchronous Reluctance Machine (SynRM) by Kostko in 1923 [3], plenty of work has been done. However, its development has been limited for some drawbacks such as low power factor, and complicated control. This machine only gained popularity in the 90's due to drive technology, which has allowed to do a great amount of work and research. As an example, in [4] a small wind turbine generation system with SynRM is detailed. Nonetheless, low power factor is still an issue to solve. To mitigate this problem, permanent magnets can be inserted into the flux barriers in order to saturate the core, yielding to higher power factor [5], [6]. Nevertheless, instead of rare-earth permanent magnet, ferrite magnets are preferred as in [7], [8] and [9], which represent a lower cost.

This report is a study design of a Ferrite Magnet-assisted Synchronous Reluctance Generator (FMaSynRG). The resulting generator is used in a simulated wind power generation system, and its basic electrical parameters are obtained. Hereafter, a brief description of its content is detailed.

- Chapter 2
  Some basic concepts and theory are shortly explained. The chapter mentions

electromagnetism rules that govern electric machinery. Also, additional characteristics of PMSG are described, and finally the voltage and torque equations in a two-axis frame is deducted.

- Chapter 3
The structure of an existing Ferrite Magnet-assisted Synchronous Reluctance Motor FMaSynRM is depicted from scratch. In addition, a detailed explanation about how to obtain its electromagnetic parameters, by means of a finite element method based software OperaFEA, is given. The simulation results are compared and contrasted with experimental results done by [9].

- Chapter 4
Two 5-MW FMaSynRG's are designed in OperaFEA. The procedure takes as a reference the size of an Internal Permanent Magnet-mounted Synchronous Generator IPMSG depicted in [10]. Then, the electromagnetic parameters are calculated according to the mentioned procedure from chapter 3. Next, the best design is selected to find power factor, phase voltage, copper and iron losses, and efficiency.

- Chapter 5
A wind power generation system is modelled. First, the required turbine characteristics for a 5-MW generator is obtained in MatLab. Next, the mathematical model of the FMaSynRG is created by considering the two-axis frame. Finally, a control system is designed in order to carry out the Maximum Torque Per Ampere (MTPA) strategy.

- Chapter 6
Some conclusions and recommendations are drawn from this work. Also, related topics are proposed as future work in order to encourage the optimization of this kind of machines.

Chapter 2

Basic Principles

In order to have a better understanding of this project, some basic theory is briefly explained in this chapter.

2.1 Laws of Electromagnetism

The Maxwell's equations (2.1 to 2.4) are the base of the fundamental theory of electromagnetic fields. In this section they are presented in the form that is most useful from the application point of view [11].

$$\nabla \cdot \overrightarrow{D} = \rho_v \qquad or \qquad \int_s \overrightarrow{D} \cdot \overrightarrow{ds} = \int_v \rho_v dv \tag{2.1}$$

$$\nabla \cdot \overrightarrow{B} = 0 \qquad or \qquad \int_s \overrightarrow{B} \cdot \overrightarrow{ds} = 0 \tag{2.2}$$

$$\nabla \times \overrightarrow{E} = -\frac{\partial \overrightarrow{B}}{\partial t} \qquad or \qquad \oint_c \overrightarrow{E} \cdot \overrightarrow{dl} = -\int_s \frac{\partial \overrightarrow{B}}{\partial t} \cdot \overrightarrow{ds} \tag{2.3}$$

$$\nabla \times \overrightarrow{H} = \overrightarrow{J} + \frac{\partial \overrightarrow{D}}{\partial t} \qquad or \qquad \oint_c \overrightarrow{H} \cdot \overrightarrow{dl} = \oint_s \overrightarrow{J} \cdot \overrightarrow{ds} + \int_s \frac{\partial \overrightarrow{D}}{\partial t} \cdot \overrightarrow{ds} \tag{2.4}$$

where:
ρ_v is the volume charge density in [C/m^3]
$\overrightarrow{D}$ is the electric flux density in [C/m^2]
$\overrightarrow{B}$ is the magnetic flux density in [T]
$\overrightarrow{E}$ is the electric field intensity in [V/m]
$\overrightarrow{H}$ is the magnetic field intensity in [A/m]
$\overrightarrow{J}$ is the volume current density in [A/m^2]

Due to the law of conservation of charge, the above equations are related among each other. This law is depicted by the equation of continuity (2.5).

$$\nabla \cdot \overrightarrow{J} = -\frac{\partial \rho_v}{\partial t} \tag{2.5}$$

Additionally, it is important to take into account the Lorentz force equation (2.6), which defines the force experienced by a charge q moving with a velocity $\overrightarrow{v}$ through an electric field $\overrightarrow{E}$ and a magnetic field $\overrightarrow{B}$.

$$\overrightarrow{F} = q(\overrightarrow{E} + \overrightarrow{v} \times \overrightarrow{B}) \tag{2.6}$$

The derived fields $\overrightarrow{D}$ and $\overrightarrow{B}$ are tied to the fundamental fields $\overrightarrow{E}$ and $\overrightarrow{H}$ by the permitivity ϵ and the permeability μ respectively, as it is shown in Equation 2.7 and Equation 2.8.

$$\overrightarrow{D} = \epsilon \overrightarrow{E} = \epsilon_r \epsilon_0 \overrightarrow{E} \tag{2.7}$$

$$\overrightarrow{B} = \mu \overrightarrow{H} = \mu_r \mu_0 \overrightarrow{H} \tag{2.8}$$

where ϵ_r is the dielectric constant and μ_r is the permeability of the medium. ϵ_0 and μ_0 are the permittivity and the permeability of free space, whose values are defined in the Equations 2.9 and 2.10.

$$\epsilon_0 = \frac{10^{-9}}{36\pi} \quad [F/m] \tag{2.9}$$

$$\mu_0 = 4\pi \cdot 10^{-7} \quad [H/m] \tag{2.10}$$

2.1.1 Induced Electromotive Force

Faraday's law of induction states that a time-varying magnetic field generates a electromotive force (emf) that sets up a current in a closed circuit. This emf arises from conductors that are moving in a constant magnetic field, or are exposed to changing magnetic fields. In the first case, this induced voltage is known as the motional emf, the speed voltage, or the emf induced by flux-cutting action [11], since the conductor is moving with a velocity $\overrightarrow{v}$ in a magnetic field $\overrightarrow{B}$ and it is found by Equation 2.11.

$$e_m = \oint_c (\overrightarrow{v} \times \overrightarrow{B}) \cdot \overrightarrow{dl} \tag{2.11}$$

In the second case, the third Maxwell's equation (2.3) represents a special case of Faraday's law, as it describes how to calculated the transformer emf due to a changing magnetic field. That is,

$$e_t = -\int\limits_s \frac{\partial \overrightarrow{B}}{\partial t} \cdot \overrightarrow{ds} \tag{2.12}$$

The total induced emf must be equal to the sum of the transformer and motional emf's. Equation 2.13 represents the mathematical definition of the Faraday's law, but it can be written in a concise form as in depicted in Equation 2.14,

$$e = -\int\limits_s \frac{\partial \overrightarrow{B}}{\partial t} \cdot \overrightarrow{ds} + \oint\limits_c (\overrightarrow{v} \times \overrightarrow{B}) \cdot \overrightarrow{dl} \tag{2.13}$$

$$e = -\frac{d\phi}{dt} \tag{2.14}$$

where

$$\phi = \int\limits_s \overrightarrow{B} \cdot \overrightarrow{ds} \tag{2.15}$$

is interpreted as the flux passing through a loop with one turn as it is illustrated in Figure 2.1. If there are N turns in a loop, the induced emf is N times as much,

$$e = -N\frac{d\phi}{dt} = -\frac{d\lambda}{dt} \tag{2.16}$$

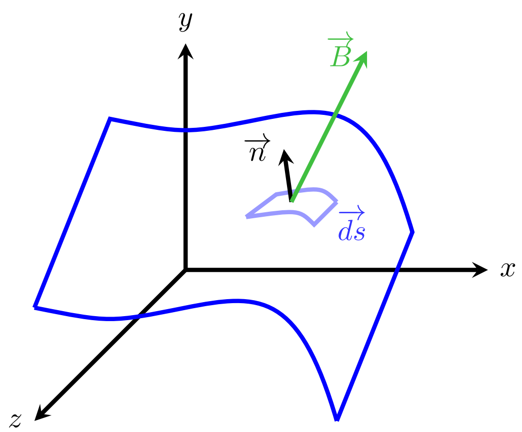

Figure 2.1: Magnetic flux density vector and normal to the surface

2.1.2 Ampere's Circuital Law

Ampere's circuital law states that the line integral of the magnetic field intensity about any closed path is equal to the total current enclosed. The latter is equal to the sum of the conduction current and the displacement current, as it is expressed in the fourth Maxwell's equation (2.4). In the case of low frequencies, the displacement current can be neglected; thus, the Equation 2.17 acts as a simplified expression of the Ampere's circuital law.

$$\oint_c \overrightarrow{H} \cdot \overrightarrow{dl} = \int_s \overrightarrow{J} \cdot \overrightarrow{ds} = I_{enc} \tag{2.17}$$

2.1.3 Magnetic Potentials

2.1.3.1 Scalar Magnetic Potential

It can be defined from the current distribution a scalar magnetic potential whose negative gradient determines the magnetic field intensity.

$$\overrightarrow{H} = -\nabla V_m \tag{2.18}$$

Having neglected the displacement current from the fourth Maxwell's equation (2.4), and considered the curl of the gradient of any scalar is identically zero, the current density must be zero ($\overrightarrow{J} = 0$) throughout the region in which the scalar magnetic potential is so defined [12].

$$\nabla \times \overrightarrow{H} = \overrightarrow{J} = \nabla \times (-\nabla V_m) = 0 \tag{2.19}$$

The scalar magnetic potential is evidently the quantity whose equipotential surfaces will form curvilinear squares with the streamlines of $\overrightarrow{H}$ in Figure 2.2.

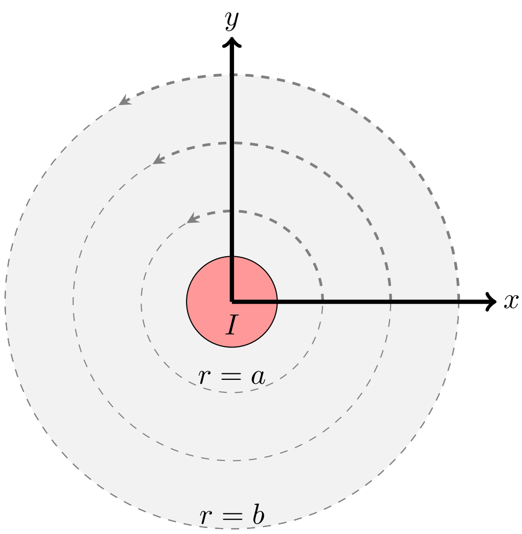

Figure 2.2: Streamlines of the magnetic field intensity about a conductor carrying a current I.

If no current is enclosed by the path of Equation 2.17, then a single-valued potential function is defined in Equation 2.20.

$$V_{m,ab} = -\int_b^a \overrightarrow{H} \cdot \overrightarrow{dl} \qquad [A] \tag{2.20}$$

2.1.3.2 Vector Magnetic Potential

Inasmuch as the divergence of the curl of any vector is zero, and by considering the second Maxwell's equation (2.2), the vector magnetic potential is deduced in Equation 2.21.

$$\nabla \cdot \overrightarrow{B} = 0$$
$$\nabla \cdot (\nabla \times \overrightarrow{A}) = 0$$

$$\overrightarrow{B} = \nabla \times \overrightarrow{A} \tag{2.21}$$

As in the Biot-Savart law (Equation 2.22), the vector magnetic potential (Equation 2.23) depends on a direct current I flowing along a filamentary conductor of which any differential length $\overrightarrow{dl}$ that is distant R from the point at which $\overrightarrow{A}$ is to be found,

$$\overrightarrow{H} = \oint \frac{I\overrightarrow{dl} \times \overrightarrow{a_R}}{4\pi R^2} \tag{2.22}$$

$$\overrightarrow{A} = \frac{\mu_0 I}{4\pi} \oint \frac{\overrightarrow{dl}}{R} \tag{2.23}$$

Hence, the vector magnetic potential allows to calculate the magnetic flux in a different form than the one shown in Equation 2.15, and it is represented in Equation 2.24.

$$\phi = \int_l \overrightarrow{A} \cdot \overrightarrow{dl} \tag{2.24}$$

Subsequently, each small section of a current-carrying conductor produces a contribution to the total vector magnetic potential, which is in the same direction as the current flows in the conductor. The vector magnetic potential is like the current distribution but fuzzy around the edges, or like a picture of the current out of focus [12]. A graphical interpretation of Equation 2.24 is shown in Figure 2.3.

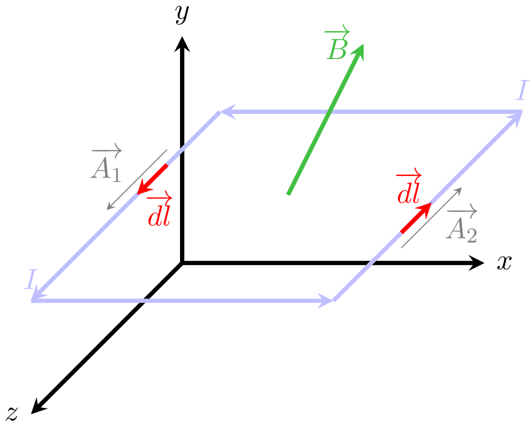

Figure 2.3: Magnetic potential vector and current-carrying conductor loop

2.1.4 Ampere's Force Law

The force exerted by the magnetic field $\overrightarrow{B}$ on the charge q that moves through this field with a velocity $\overrightarrow{v}$ is detailed in Equation 2.25.

$$\overrightarrow{F} = q\overrightarrow{v} \times \overrightarrow{B} \tag{2.25}$$

Insomuch as the current constitutes moving charges in a conductor, Equation 2.25 can be modified to be expressed in terms of the current in Equation 2.26.

$$\overrightarrow{F} = \int_c I\overrightarrow{dl} \times \overrightarrow{B} \tag{2.26}$$

From the above, the force experienced by a current-carrying conductor depends upon the magnetic field density, the current magnitude, and the conductor length. As the force acting on a conductor is maximum when the magnetic field is perpendicular to the current-carrying conductor, all rotating machines are designed to house current-carrying conductors perpendicular to the magnetic field [11].

2.1.4.1 Torque on a Current Loop

The Figure 2.4 shows one current loop oriented perpendicularly to the magnetic field. The force acting on each side of the loop can be determined by using Equation 2.26. As a result, the forces on the opposite sides of the loop are equal in magnitude but opposite in direction. Due to the fact that the lines of action of these forces are the same, the net force is zero.
In Figure 2.5, the loop is oriented in such a way that the normal of the plane makes an angle θ with the magnetic field density. The lines of action of forces acting on each side of length L_x still coincide. Hence, the net force in the z direction is still

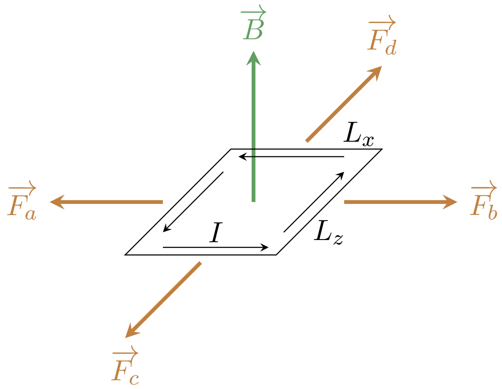

Figure 2.4: A current loop perpendicular to a uniform magnetic field density

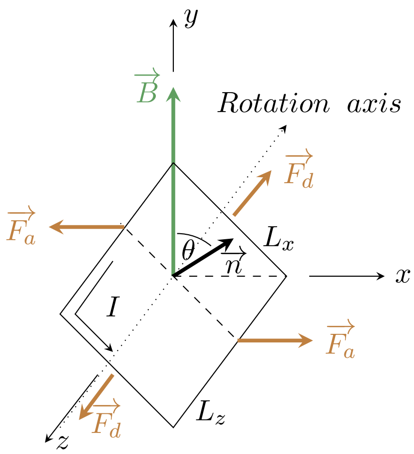

Figure 2.5: A current loop perpendicular to a uniform magnetic field density

zero. However, the lines of action of the forces acting on each side of length L_z do not coincide. If the loop is free to rotate along the z-axis, these forces tend to rotate the loop in the counterclockwise direction [11]. The forces in each conductor with length L_z are:

$$\overrightarrow{F_a} = -BIL_z\,\overrightarrow{a_x}$$
$$\overrightarrow{F_b} = BIL_z\,\overrightarrow{a_x}$$

Likewise, the torques of these conductors are:

$$\overrightarrow{T_a} = BIL_z(L_x/2)\,sin(\theta)\,\overrightarrow{a_z}$$
$$\overrightarrow{T_b} = BIL_z(L_x/2)\,sin(\theta)\,\overrightarrow{a_z}$$

If N turns are considered instead of one loop, the total torque is depicted in Equation 2.27.

$$\overrightarrow{T} = BINA_{xz}\,sin(\theta)\,\overrightarrow{a_z} \tag{2.27}$$

2.1.5 Maxwell Stress Tensor

A linear current density $\overrightarrow{K}$, can be defined in a electrical machine as a current sum flowing in a stator slot divided by the slot pitch [13]. This linear current density creates tangential field strength components on the metal surfaces, which are responsible for torque generation in rotating-field electrical machines [13]. Figure 2.6 depicts the normal and tangential magnetic field strength in an electrical machine.

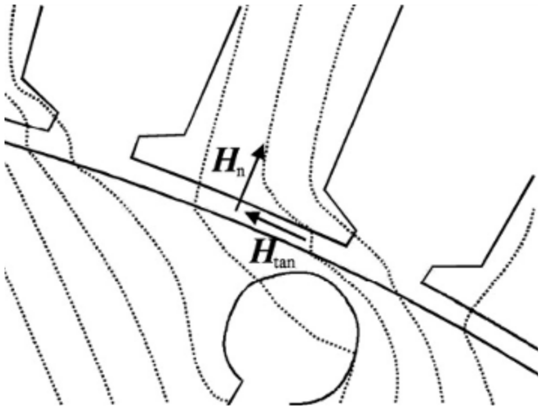

Figure 2.6: Normal and tangential component of the air-gap field strength [13]

According to Maxwell's stress theory, the magnetic field strength between objects in a vacuum brings about a stress σ_F on the object surfaces.

$$\sigma_F = \frac{1}{2}\mu_0 H^2 \tag{2.28}$$

where its normal and tangential components can be found.

$$\sigma_{F_n} = \frac{1}{2}\mu_0(H_n^2 - H_{tan}^2) \tag{2.29}$$

$$\sigma_{F_{tan}} = \mu_0 H_n H_{tan} \tag{2.30}$$

2.2 Magnetic Parameters

2.2.1 Reluctance

An analogy can be drawn from electric circuits to explain the concept of reluctance by the use of magnetic circuits. In Figure 2.7, the current flowing through the winding generates a magnetomotive force (MMF) which depends on the number of turns and

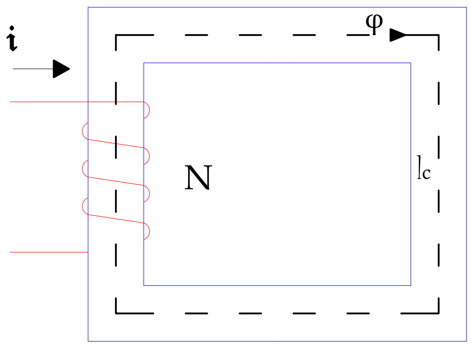

Figure 2.7: Magnetic flux established by a current-carrying coil

the current amplitude. The relationship between the MMF acting on a magnetic circuit and the magnetic field intensity is.

$$\mathcal{F} = Ni = \oint \overrightarrow{H} \cdot \overrightarrow{dl} = MMF \tag{2.31}$$

Since the core geometry is uniform, the line integral of Equation 2.31 becomes simply the scalar product of magnetic field intensity and the core length shown in Equation 2.32.

$$\mathcal{F} = Ni = H_c l_c \tag{2.32}$$

Similarly, Equation 2.15 becomes the scalar product of magnetic field density and the core cross-section area shown in Equation 2.33.

$$\phi = B_c A_c \tag{2.33}$$

Substituting Equations 2.8 and 2.33 into Equation 2.32 gives,

$$\mathcal{F} = \phi \frac{l_c}{\mu A_c} \tag{2.34}$$

The term that multiplies the flux is known as Reluctance.

$$\mathcal{R} = \frac{l_c}{\mu A_c} \tag{2.35}$$

2.2.2 Self-Inductance and Mutual Inductance

Inductance describes a coil's ability to produce flux linkage [13]. From Equation 2.16 the flux linkage of the winding is defined as,

$$\lambda = N\phi \tag{2.36}$$

The relationship between flux linkage and current is linear, then the inductance can be define as

$$L = \frac{\lambda}{i} \tag{2.37}$$

substitution of Equations 2.32, 2.34, 2.35 and 2.36 into Equation 2.37 gives

$$L = \frac{N^2}{\mathcal{R}} \tag{2.38}$$

From the magnetic circuit displayed in Figure 2.8 it can be inferred,

$$\varphi = (N_1 i_1 + N_2 i_2)\frac{\mu A_c}{l_c}$$

where φ is the resultant core flux produced by the total mmf of the two windings. Then,

$$\lambda_1 = N_1\varphi = N_1^2\left(\frac{\mu A_c}{l_c}\right)i_1 + N_1 N_2\left(\frac{\mu A_c}{l_c}\right)i_2$$

which can be written

$$\lambda_1 = L_{11} i_1 + M_{12} i_2$$

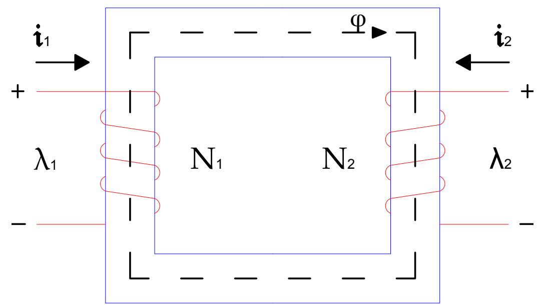

Figure 2.8: Magnetic circuit with two windings

where L_{11} is the self-inductance and M_{12} is the mutual inductance which are depicted in Equations 2.38 and 2.40 respectively.

$$L_{11} = \frac{N_1^2}{\mathcal{R}} \tag{2.39}$$

$$M_{12} = \frac{N_1 N_2}{\mathcal{R}} \tag{2.40}$$

2.3 Magnetization of Permanent Magnets

The magnetization orientation strongly influences the quality of the air gap flux density distribution and indirectly affects the power density in a given arrangement of the machine with permanent magnets [14].

2.3.1 Radial and Parallel Magnetization

The radial magnetization is along the radius in the same direction as the normal to the surface represented in Figure 2.9, while the parallel magnetization is alongside to the edges forming an angle between the magnetization vector $\overrightarrow{M}$ and the normal to the surface $\overrightarrow{n}$ which is seen in Figure 2.10.

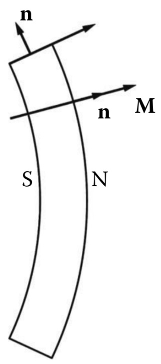

Figure 2.9: Radial magnetization [14]

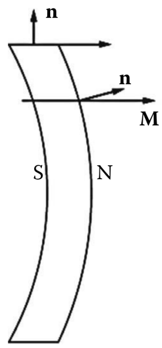

Figure 2.10: Parallel magnetization [14]

The radially magnetized magnets produce a rectangular flux density distribution in the air gap, whereas the parallel magnetized magnets cause a sinusoidal air gap flux density distribution. In the first case, the magnet flux leaves the permanent magnet and enters the stator in normal direction to their surfaces. Thus, the air gap flux and its density are maximum and remain uniformly constant across the magnet. In the second case, the normal component of the flux density vector that enters the stator is proportional to sine of the angle between the x-axis and the $\overrightarrow{M}$ [14].

2.3.2 Halbach Array of Permanent Magnets

The Halbach arrangement is a combination of one radial magnet array and one azimuthal magnet array, whose sum brings about the flux distribution shown in Figure 2.11. The flux lines on the top are very small compared to the ones in the bottom, implying that back iron is not required in the top part of the Halbach array.

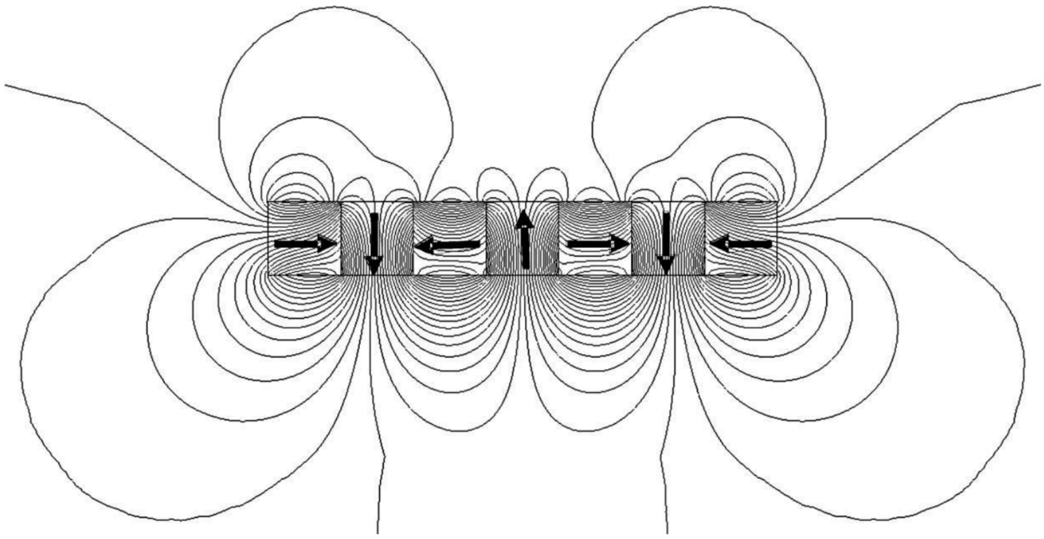

Figure 2.11: Combination of radial and azymuthal magnet arrays to make a Halbach array [14]

Clockwise orientation sequence (seen from left to right) gives inward flux distribution, which is used in machines with outer rotors and inner stators (see Figure 2.12). Likewise, anticlockwise orientation sequence gives outward flux distribution and it is used for conventional machines (see Figure 2.13).

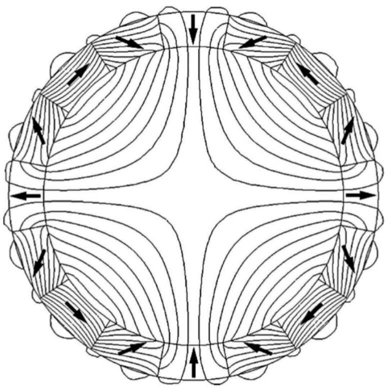

Figure 2.12: Halbach inward flux distribution [14]

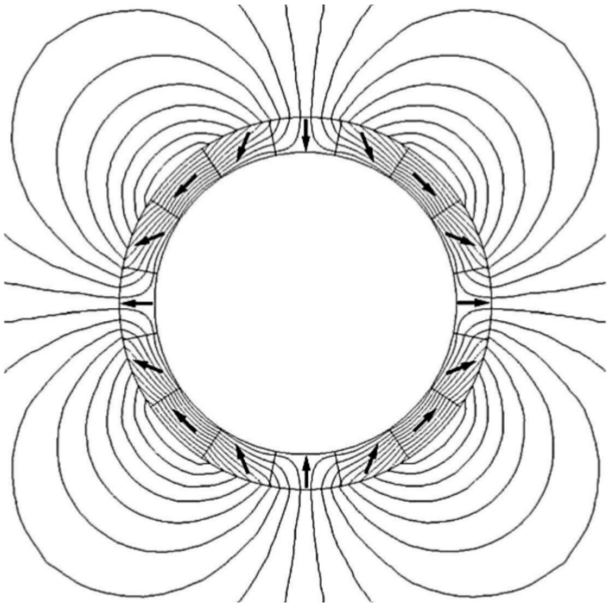

Figure 2.13: Halbach outward flux distribution [14]

In both figures, the halbach arrays present four magnet segments per pole, whose flux density distributions are almost sinusoidal when the ripples, due to the slot opening of the stator laminations, are ignored. To attain a smoother sinusoidal flux density waveform, the number of magnet segments per pole must be increase; thus, the torque ripple is reduced.

2.4 Synchronous Reluctance Machine

The physical principle of reluctance torque lies on the asymmetric geometry of a magnetic object exposed to a magnetic field. As it shown in Figure 2.14, the d-axis of the object has a longer length than in q-axis. When a flux φ is applied, the d-axis aligns with the direction of the flux, which bring about torque. If the flux results from a rotating current vector, the magnetic object rotates with the same angular speed than the current vector.

A synchronous reluctance machine (SynRM) can be considered as the simplest electrical rotating machine since rotor conductors are not required. The torque is produced as a result of the magnetic rotor saliency, which aligns with the stator flux generated by the stator current vector in order to maximize flux linkages [15], as it is illustrated in Figure 2.15.

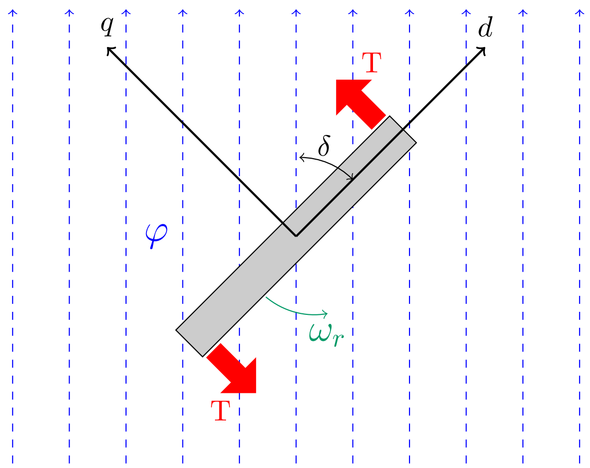

Figure 2.14: Physical principle of reluctance torque

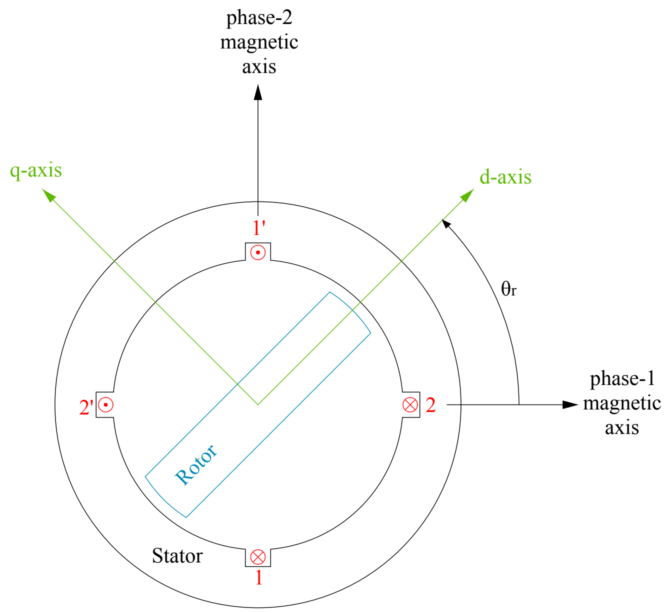

Figure 2.15: Basic stator-rotor structure of SynRM

2.5 Voltage and Torque Equations

In order to derive the expressions of a SynRM, a two-pole three-phase permanent magnet ac machine is utilized, as it is illustrated in Figure 2.16. The d-axis is aligned with the phase-a MMF, and the q-axis is leading 90°. The voltage equations in *abc* frame are

$$v_{abc} = R_s\, i_{abc} + \frac{d}{dt}\lambda_{abc} \tag{2.41}$$

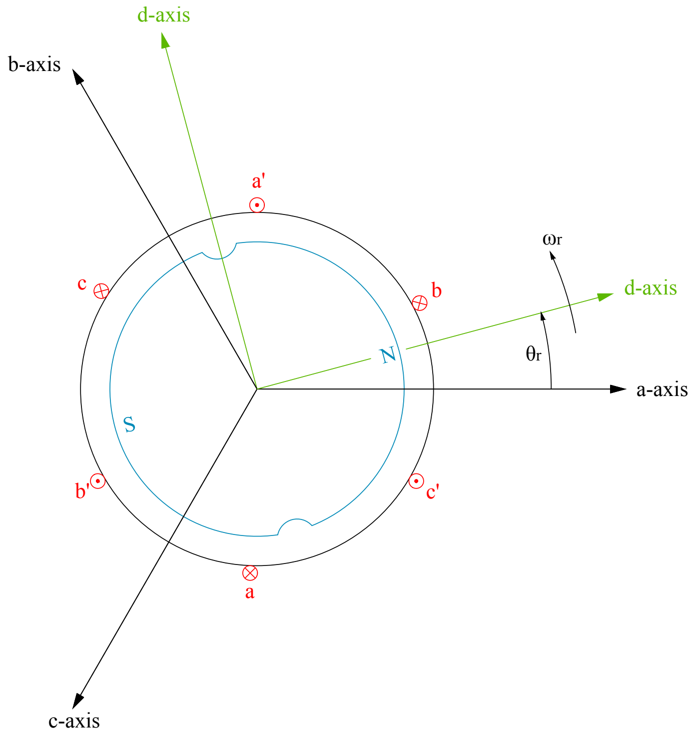

Figure 2.16: Two-pole three-phase permanent magnet AC machine

where

$$f_{abc} = \begin{bmatrix} f_a & f_b & f_c \end{bmatrix}$$

$$R_s = \begin{bmatrix} r_s & 0 & 0 \\ 0 & r_s & 0 \\ 0 & 0 & r_s \end{bmatrix}$$

and the flux linkages are

$$\lambda_{abc} = L_s \, i_{abc} + \lambda_\theta$$

Since L_s and λ_θ depend on the rotor position, the equations become complicated. Hence, the equations are represented in a rotating dq-axis frame as it is explained in [16]. The required transformation frame for the inductances uses a simple approach detailed in [17]. As a result, the equivalent voltage expression is given in Equation 2.42.

$$v_{dq0} = R_s i_{dq0} + \omega_r \lambda_{qd0} + \frac{d}{dt}\lambda_{dq0} \tag{2.42}$$

where

$$\lambda_{dq0} = \begin{bmatrix} L_{ls} + L_{md} & 0 & 0 \\ 0 & L_{ls} + L_{mq} & 0 \\ 0 & 0 & L_{ls} \end{bmatrix} \begin{bmatrix} i_d \\ i_q \\ i_0 \end{bmatrix} + \begin{bmatrix} \lambda_{mpm} \\ 0 \\ 0 \end{bmatrix}$$

$$L_d = L_{md} + L_{ls}$$
$$L_q = L_{mq} + L_{ls}$$

$$\lambda_d = L_d i_d + \lambda_{mpm} \tag{2.43}$$
$$\lambda_q = L_q i_q \tag{2.44}$$
$$\lambda_0 = L_{ls} i_0 \tag{2.45}$$

then, the voltage is expressed as the following system of equations:

$$v_d = r_s i_d - \omega_r L_q i_q + \frac{d}{dt}(L_d i_d) \tag{2.46}$$
$$v_q = r_s i_q + \omega_r L_d i_d + \omega_r \lambda_{mpm} + \frac{d}{dt}(L_q i_q) \tag{2.47}$$
$$v_0 = r_s i_0 + \frac{d}{dt}(L_{ls} i_0) \tag{2.48}$$

Additionally, the three-phase input power is calculated in *abc* frame by the sum of the product between the voltage and current in each phase.

$$P_{abc} = v_a i_a + v_b i_b + v_c i_c \tag{2.49}$$

In the same way, the power can be expressed in *dq* frame.

$$P_{dq0} = \frac{3}{2}(v_q i_q + v_d i_d + 2 v_0 i_0) = P_{in} \tag{2.50}$$

The electromagnetic torque multiplied by the rotor mechanical angular velocity results in the output power. Ideally, the output power is equal to the input power.

$$P_{out} = T_e \left(\frac{\omega_r}{\mathfrak{p}} \right) \tag{2.51}$$

where $\mathfrak{p}$ is the number of pair-poles. By substituting Equation 2.51 into Equation 2.50 the output power follows

$$\begin{aligned} T_e \left(\frac{\omega_r}{\mathfrak{p}} \right) &= \frac{3}{2} r_s (i_q^2 + i_d^2 + 2 i_0^2) \\ &+ \frac{3}{2} \left(i_d \frac{d}{dt} \lambda_d + i_q \frac{d}{dt} \lambda_q + 2 i_0 \frac{d}{dt} \lambda_0 \right) \\ &+ \frac{3}{2} (\lambda_d i_q - \lambda_q i_d) \omega_r \end{aligned} \tag{2.52}$$

The first term of Equation 2.52 represents the ohmic power loss, and the second one is the change of stored magnetic energy. By dividing the Equation 2.52 by the angular speed ω_r, the thrid term allows to find the electromagnetic torque displayed in Equation 2.54.

$$T_e = \frac{3}{2}\mathfrak{p}(\lambda_d i_q - \lambda_q i_d)\omega_r \tag{2.53}$$

Additional substitution of Equation 2.44 and Equation 2.43 into Equation 2.54 results in the electromagnetic torque equation in dq frame.

$$T_e = \frac{3}{2}\mathfrak{p}(\lambda_{mpm} i_q + (L_d - L_q) i_q i_d) \tag{2.54}$$

Chapter 3

Primary Design Procedure

This chapter aims to explain how to determine the parameters of a electrical machine by the finite element method. Additionally, the effects of the geometry, materials and stator winding configurations on these machine parameters are analyzed. The idea is to show how to obtain this data and verify its accuracy. To carry out this task, the results are compared with the experimental data of an existing SynRM, whose main characteristics are detailed in Table 3.1. Thus, this chapter is divided in three sections. First, the physical and electromagnetic features of the machine are depicted. The dimensions and materials are selected based on the existing SynRM. Then, the magnetic flux, torque and inductance are calculated by the finite element analysis, whose results are compared with the existing machine. Finally, a conclusion is drawn to justify the veracity of this procedure.

Table 3.1: Grundfos SynRM [9]

Parameter	Value
Active Power	13 kW
Frequency	50 Hz
Rated speed	3000 rpm
pair-pole number	2

3.1 Geometry of a existing SynRM

Even though there are some techniques to design the size and dimensions of the stator and rotor based on a specific rated power, the geometry of an existing machine is explained and utilized in this chapter. Thus, the stator structure of this particular machine is depicted hereinafter. Therefore, the actual design process is explain in chapter 4.

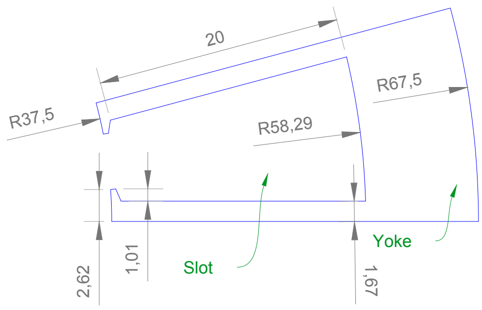

Figure 3.1: Dimensions of one stator slot

3.2 Stator Geometry and Dimensions

The structure of the stator is composed by a high-permeability core and armature windings. The former has a number of slots where the coils are placed, in a distributed-, integral- or fractional-slot winding configuration [18]. The slot area depends on the number of winding turns, which has a direct relationship with the machine torque capability. As a result, it is worthy to described each part separately.

3.2.1 Stator Core

The existing machine counts on a laminated stator with 24 slots symetrically distributed, whose magnetic sheet properties are detailed in Appendix A. The slot cross-sectional area S_{slot} houses N winding turns with a fill factor k_f, which is determined by Equation 3.1

Table 3.2: Stator dimensions and general characteristics

Parameter	Value
Stator outer diameter	135 mm
Stator inner diameter	75 mm
Stack length	100 mm
Number of slots	24
Magnetic sheet	M270-35A
Slot cross-sectional area	188.25 mm^2
Wire diameter	0.77 mm

$$k_f = \frac{N \cdot S_c}{S_{slot}} \tag{3.1}$$

where S_c is the conductor cross-sectional area. The wire diameter of the stator winding is 0.77 mm, 190 turns are placed in each slot, and the slot cross-sectional area is equal to 188.25 mm^2; consequently, the fill factor is 0.47. The structure dimensions are detailed in Figure 3.1, and the main characteristics are listed in Table 3.2.

3.2.2 Stator Windings

In the existing machine are placed two identical three-phase windings connected in parallel. Each phase winding per pole-pair has two equivalent coils connected in series, and each equivalent coil contains two coils in parallel. As a result, each slot houses two coils with 95 turns each. The equivalent circuit per phase is shown in Figure 3.2, Where L_{95} represents one coil with 95 turns.

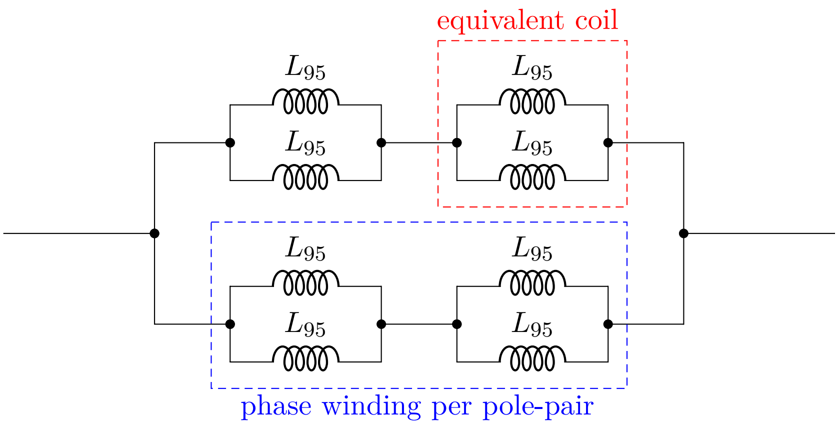

Figure 3.2: Coil arrangement per phase

Additionally, a distributed-slot winding configuration is established, where the number of slots/pole/phase (q) is equal to two. Since the 24 slots is divided by 4 poles and three phases [18]. Moreover, a simple-layer winding arrangement has been chosen, where their coils are full pitched. This winding configuration creates a single and understandable layout, which is depicted in Figure 3.3.

3.3 Rotor Geometry and Dimensions

Likewise as the stator, the rotor structure is not designed, but chosen from a topology proposed in [19], where a moulding technology of ferrite magnet is described. With this structure, the complete flux barrier is filled with melted ferrite magnet, which

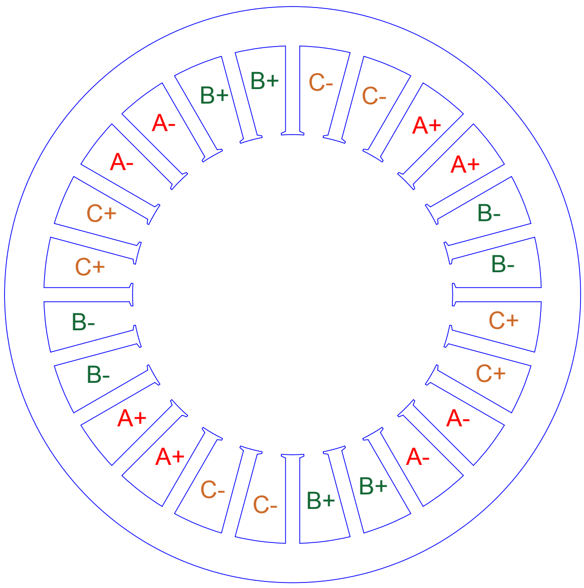

Figure 3.3: One-layer distributed-slot winding configuration

cannot be done with pre-formed regular-shaped magnet pieces. As a result, the flux barriers do not have to be designed into specific shapes to house the magnet pieces, and the torque performance does not depend on this restriction.

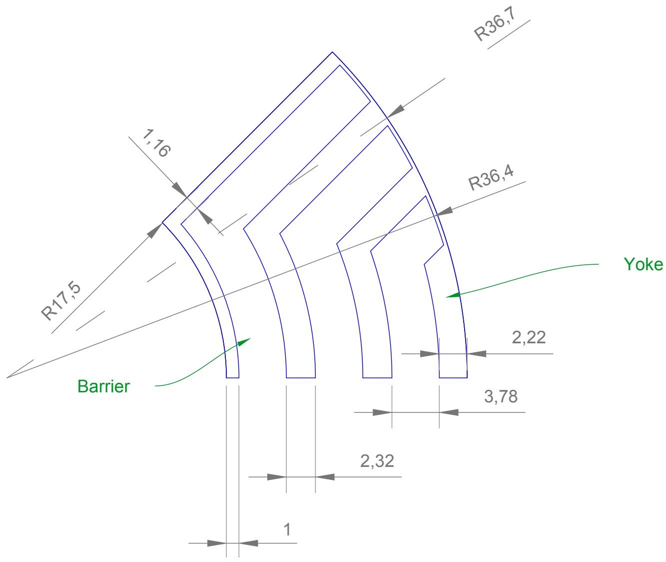

Figure 3.4: Rotor dimensions

3.3.1 Rotor Core

The rotor structure is composed by two pole-pairs, and each pole is formed by a non-salient yoke with three flux barriers. According to [10], there is not considerable improvement if the number of flux barriers is greater than 3, hence savings in material and processing costs. Moreover, this asymmetric structure, as it is explained in [20], maximizes the average torque and minimizes the torque ripple. The rotor geometry is depicted in Figure 3.4, as well as its complete schematic in Figure 3.5. Additionally, its main characteristics and dimensions are listed in Table 3.3.

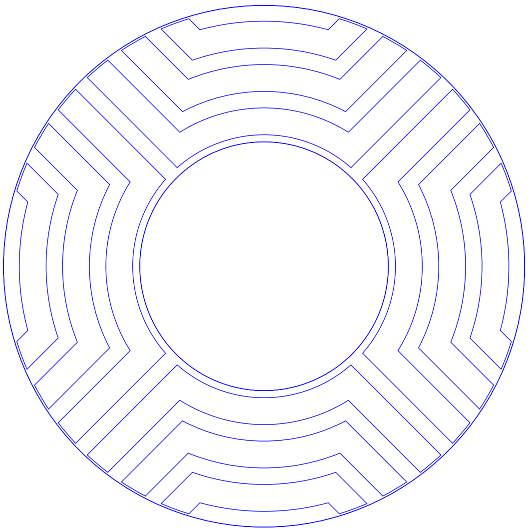

Figure 3.5: Complete rotor schematic

Table 3.3: Rotor dimensions and general characteristics

Parameter	Value
Rotor outer diameter	73.4 mm
Rotor inner diameter	35 mm
Stack length	100 mm
Flux barrier length	3.78 mm
Magnetic sheet	M270-35A
Number of poles	4

3.3.2 Ferrite Magnets

As it was mentioned above, the flux barriers are filled with melted ferrite magnet, which results from mixing ferrite magnet powder and binder. This material is presented in pellets (see Figure 3.6) that are heated to transform them in liquid state and subsequently injected into the rotor flux barriers of the Figure 3.7. Afterwards, the moulded rotor is placed inside a Halbach magnet ring with inward flux distribution, similar to Figure 2.12, hence the crystals are oriented to the desired magnetic field. A more detailed procedure of the moulding technology is explained in [19]. Once completed the process, the SynRM now is assisted by ferrite magnet, hereinafter is referred as FMaSynRM.

Figure 3.6: Pellets of mixture of ferrite magnet powder and binder [19]

Figure 3.7: Real rotor prototype

In order to reproduce the rotor magnetic flux in the finite element method, the ferrite magnet magnetization angle is required. Since this structure presents an asymmetric form, the assignment of this angle is not a straightforward task. For this reason, the rotor structure is drawn along with an inward Halbach ring configuration where the magnetic properties of Appendix A are considered. The Halbach ring consists of 16 magnet pieces, whose magnetization angle distribution is set according to Figure 3.8. This Halbach configuration generates four poles through the rotor core as it shown in Figure 3.9.

In addition, each rotor flux barrier is divided in small sub-regions, whose inner material is assigned as air instead of the ferrite magnet. Under these conditions, it can be seen in Figure 3.10 that each sub-region is subjected to a specific magnetization angle, which defines the direction of the field lines that pass through it. Hence, each sub-region has a different magnetization angle, whose values are saved to be set in the FMaSynRM model.

Having finished the rotor and stator geometry, defined the different materials of the

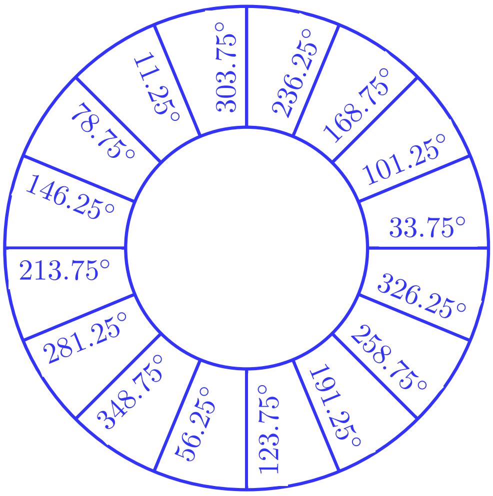

Figure 3.8: Halbach ring magnetization angle distribution

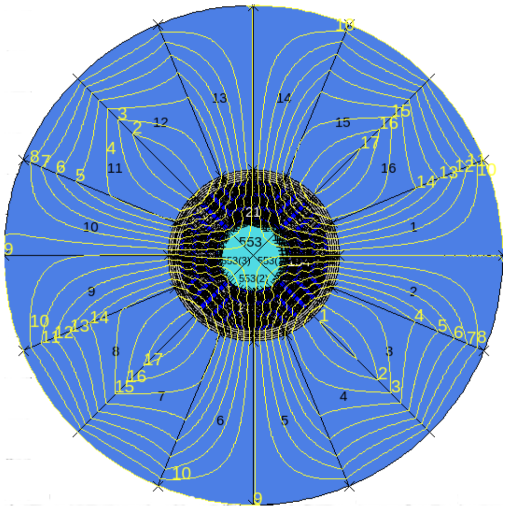

Figure 3.9: Halbach ring and magnetic field lines through the rotor

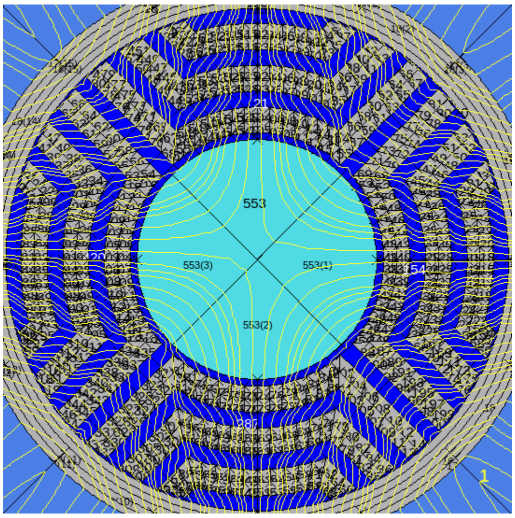

Figure 3.10: Rotor magnetic field lines

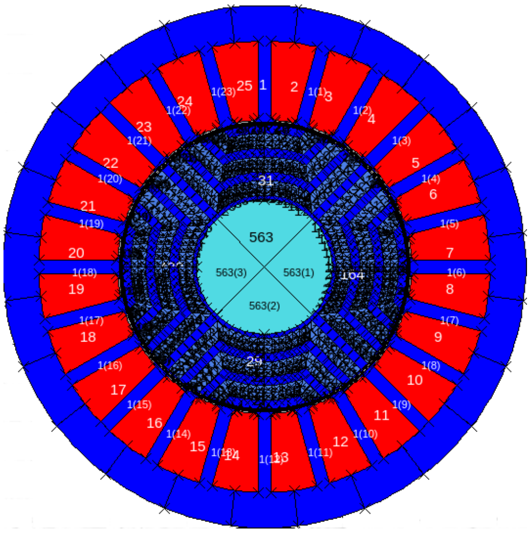

Figure 3.11: FMaSynRM model

model, and set the magnetization angles in the sub-regions of the flux barriers with ferrite magnets, the FMaSynRM model is represented in Figure 3.11.

3.4 Calculation of Electromagnetic Parameters

Once the FMaSynRM model is established in the software based on finite element method OperaFEA, its main parameters are calculated and compared with the experimental results given by [9]. By doing so, it can justify if the proceeding and approach in the simulation represent the actual performance of the FMaSynRM.

3.4.1 Magnetic Flux

In order to find the induced magnetic flux on the stator windings, no current is set on them, thence no armature reaction is seen. The magnetic flux is measured in each position that the rotor takes, which rotates in steps of 1.5°. Due to the two pole-pair, the rotor has to take 120 steps until a cycle is completed. According to Figure 3.3 and Figure 3.11, the slot numbers that house the phase-a windings are 4, 5, 16, 17 for the positive direction current (perpendicular out of the page), and 10, 11, 22, 23 for the negative direction current (perpendicular into the page). Correspondingly, for phase b the slot numbers are 12, 13, 24, 25 for positive current, and 6, 7, 18, 19 for negative current. Consequently, the positive slot numbers for phase c are 8, 9, 20, 21 and the negative ones are 2, 3, 14, 15. As it was seen in Figure 3.2, in each slot-pair, for instance 4 and 10 for phase a, there are two coils connected in parallel creating an equivalent coil. Hence, the induced magnetic flux is the same in these two coils, it is enough to measure the magnetic flux in one of them. As a result, the slot is divided into two identical areas as it is depicted in Figure 3.12.

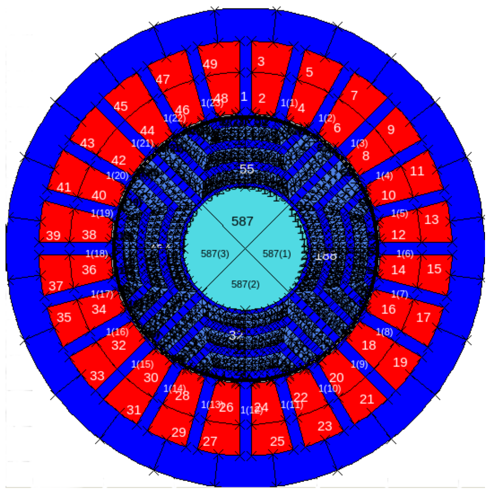

Figure 3.12: FMaSynRM final model

Additionally, the equivalent coil is connected in series with a similar one, where the magnetic flux is also measured in one of the two coils connected in parallel. These two taken values are added up and multiply by four, since the coil arrangement appears as a set of eight coils divided by four branches connected in parallel, and each branch with two coils connected in series. An identical analysis is done for phase b and c. The resultant magnetic fluxes are shown in Figure 3.13, whose fundamental peak value is equal to 0.19442 Wb.

The fundamental magnetic flux peak value given by [9] is 0.180 Wb, which brings about an relative error of 8%. This result represents a good approximation of the

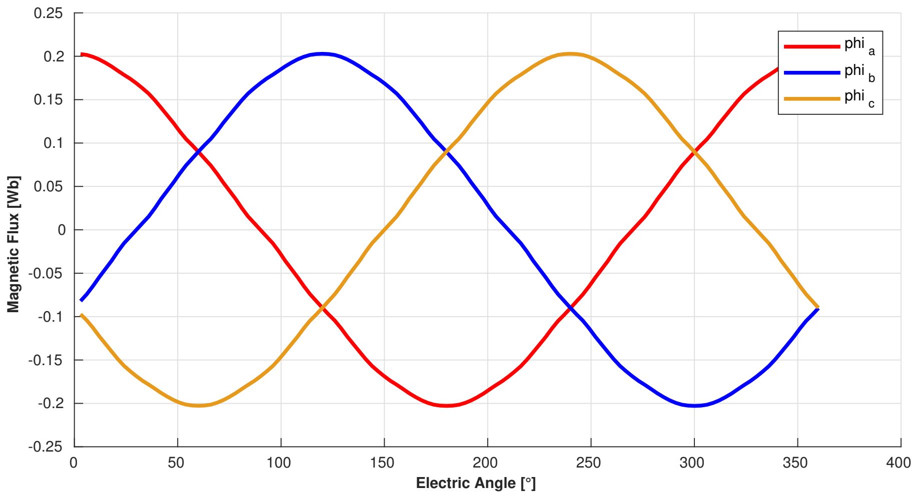

Figure 3.13: Induced magnetic flux in the stator windings

model if it considered the following reasons for this mismatch:

- The leakage flux at the winding endings is not considered in the two-dimensional analysis.
- The stator geometry is an approximation. The real slot and tooth dimensions are confidential information.
- The magnetic properties of the ferrite and binder mixture is not totally accurate.

3.4.2 Torque

For the torque calculation, the air gap of the FMaSynRM is divided in five regions (see Figure 3.14) and two different methods are proposed. The first one calculates the torque around a circular arc, and the second one evaluates the integral over a region, where the values of tangential and radial flux densities are collected to obtain the torque by applying the Maxwell stress tensor Equation 2.30. The resultant torque is attained from the average value of the outcomes.
According to Equation 2.27, the generated torque by the machine depends on the rotor position. If the Maximum Torque Per Ampere (MTPA) strategy control is chosen, finding the peak value is required. To start, the rotor d-axis is aligned with the phase-a magnetomotive force (MMF) when the angular position is zero. As a result, the north pole is aligned with the current space vector. Next, the angular position of the current space vector changes in steps of 3° (1.5° mechanical steps) and the rotor position is kept. The outcome for a current density equals 4.4 A/mm^2 is described in Figure 3.15, where the peak value equal to 8.871 Nm is reached at 129°,

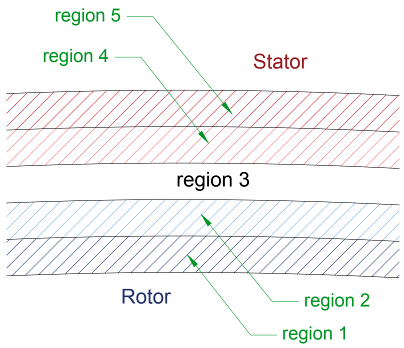

Figure 3.14: Five air gap regions for torque calculation

when there is a stator current of 8.1961 A. Furthermore, the torque Equation 2.54 is also evaluated. Even though there is a mismatch among the different calculation methods, it can be seen that the peak value occurs at the same electric angle. Thus, in order to reach the maximum torque per ampere with a current density of 4.4 A/mm^2, the current space vector and the d-axis have to form an angle of about 129°. In addition, Figure 3.16 shows the maximum torque that the machine can achieve with different current densities, which can be also be represented as a function of the phase current as it is depicted in Figure 3.17.

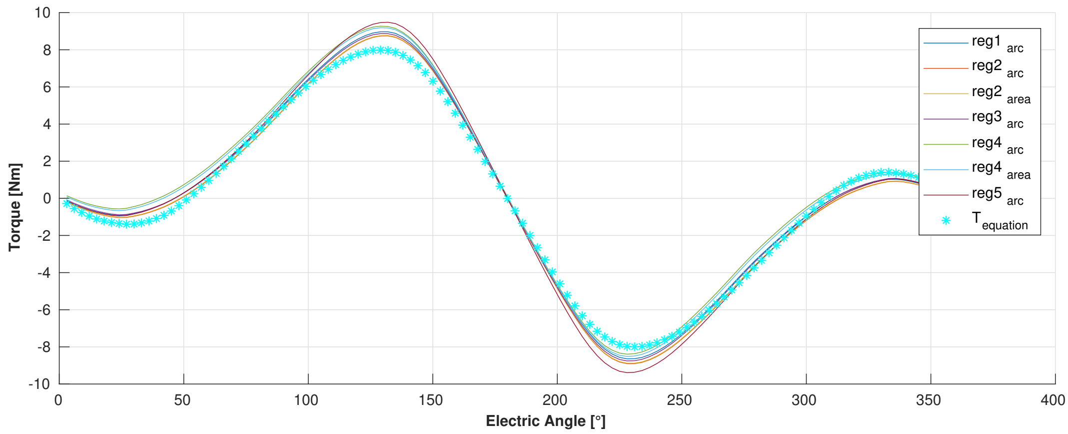

Figure 3.15: Torque waveform with blocked rotor and 4.4 A/mm^2

3.4.3 Inductance

Regarding the torque equation, the d- and q-axis inductances determine the amplitude of the reluctance torque. The greater the salient ratio L_q/L_d, the higher the torque amplitude . Additionally, this salient ratio has an important impact on the power factor of the machine [21], [22], [23]. By assuming the pessimistic case, where

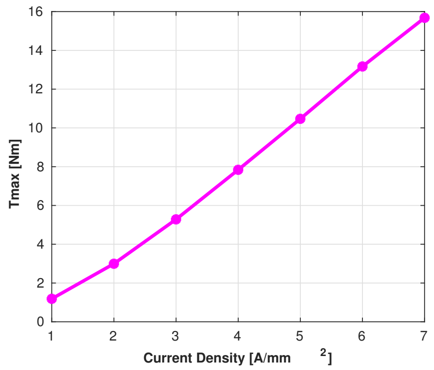

Figure 3.16: Maximum Torque vs Current Density

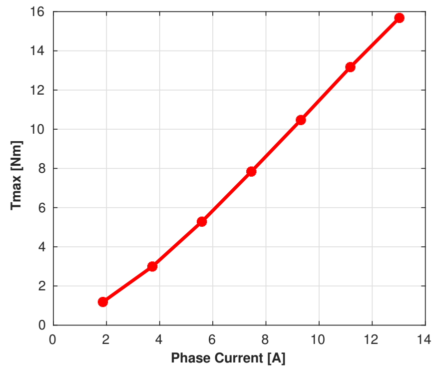

Figure 3.17: Maximum Torque vs Phase Current

there is not voltage drop due to any resistive component, the power factor as a function of the salient ratio is depicted in Equation 3.2 [24]. The details of how to obtain this expression are in Appendix B.

$$cos(\phi) = \frac{\frac{L_q}{L_d} - 1}{\frac{L_q}{L_d} + 1} = \frac{L_q - L_d}{L_q + L_d} \tag{3.2}$$

By aligning the d-axis with the current space vector, and increasing the magnitude from this latter, the inductance in the d-axis L_d is found just by evaluating the linear relationship between the magnetic flux and the current (Equation 2.37). Similarly, to find the inductance in the q-axis L_q the same procedure is followed, except that the q-axis is aligned with the current space vector. The results of these two inductances by simulation and experimental work done by [9] are illustrated in Figure 3.18 and

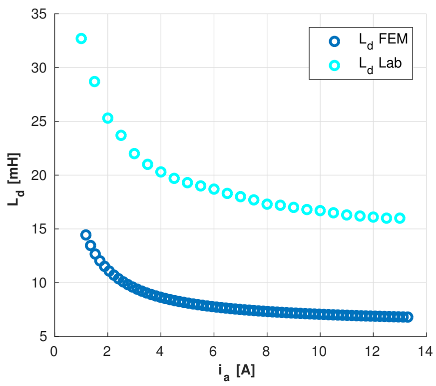

Figure 3.18: d-axis inductance of FMaSynRM

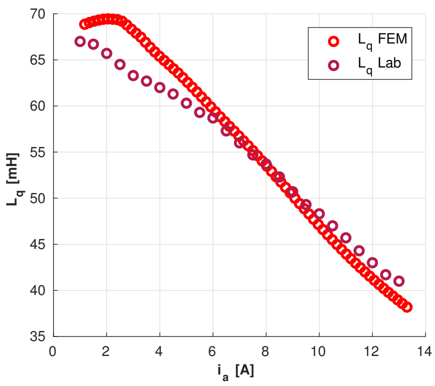

Figure 3.19: q-axis inductance of FMaSynRM

Figure 3.19.

Once again, a considerable mismatch is shown due to assuming some data. However, the outcome from OperaFEA shows a salient ratio around 5, which represents the actual value in order to reach the required torque. On the other hand, the experimental values give a salient ratio about 2 that cannot perform a proper operation.

Even though there are some mismatches in the results and the existing data, the goal of this chapter was to present the steps to follow to measure the electromagnetic parameters by using the finite element method. It should be emphasized that certain approximations were used to carry out this analysis, bringing with it satisfactory results.

Chapter 4

Design and Optimization of FMaSynRG

In this chapter, the stator and rotor are sized for a 5-MW Ferrite Magnet assisted Synchronous Reluctance Generator (FMaSynRG). To make shorter and easier the design, the materials for the FMaSynRM of the previous chapter are kept. Besides, the stator inner and outer diameters are taken from [10], so that the results are compared with an Interior Permanent Magnet Synchronous Generator (IPMSG). Basically, the design process for the stator follows the concepts of [13], and in the case of the rotor design, it takes the criteria given by [10], [9] and [24]. Moreover, the electromagnetic parameters are calculated by finite element analysis as it was realized in chapter 3, and the back-EMF is found based on the approximation given in [25] and compare with a mathematical approach.

4.1 Geometry and Dimensions of FMaSynRG

According to [13], machine design is a rather complicated iteration process, which can be described in four main steps.

1. The initial dimensions are selected by considering the power that the machine requires to generate, or based on the copper loss per stack outer surface as it is explained in [26].
2. The geometry and electrical components are sized to satisfy the needed voltage, current and torque.
3. A proper cooling system is chosen.
4. If the cooling system is not efficient enough, the dimensions of the machine can be increased, the materials are changed, or another cooling system is selected.

The design of this specific machine takes as a reference the size of the 5-MW Internal Permanent Magnet Synchronous Machine (IPMSM) described in [10], and the basic structure of the FMaSynRM from the previous chapter. Table 4.1 lists the data that is used as starting point of this design. However, these dimensions are modified, and the electromagnetic parameters of the new model are compared with the original machine later on.

Table 4.1: FMaSynRG reference data

Parameter	Value
Rated Power	5 MW
Frequency	50 Hz
Rated speed	1500 rpm
Pair-pole number	2
Outer stator diameter	1100 mm
Inner stator diameter	758 mm
Inner rotor diameter	400 mm

It is important to point out that the dimensions are used as a reference, and cannot represent the final ones. To start the sizing procedure, a brief description of the rotor geometry is given hereafter.

4.1.1 Rotor Design

Basically, the rotor structure described in chapter 3 is kept and coupled to the generator size. To define the latter, two following criteria are considered.

R1: The flux barrier width, the space between the barriers and the magnet coverage are taken from the optimized analysis of a 3-layer Permanent Magnet-assistes Synchronous Machine (PMaSynRG) given by [10].

R2: The proportional dimensions of the FMaSynRM (chapter 3) are kept by a simple rule of three.

4.1.1.1 First rotor design approach

In the case of the rotor design number 1 (R1), if the asymmetric geometry is not considered, the equivalent rotor structure for a 4-pole SynRM is illustrated in Figure 4.1.

Figure 4.2 shows the same rotor with asymmetric flux barriers. It can be seen that there is an appreciable amount of unused core. Thus, the rotor diameter is reduced until the space between the shaft and the inner flux barrier is slightly lower than the space between flux barriers, thence saving material. The final rotor geometry is illustrated in Figure 4.3

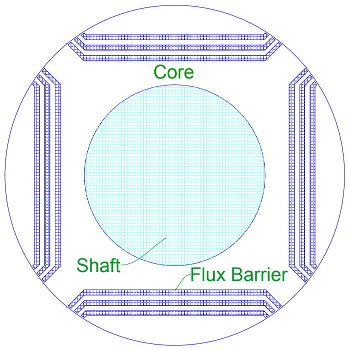

Figure 4.1: Straight flux barrier rotor topology

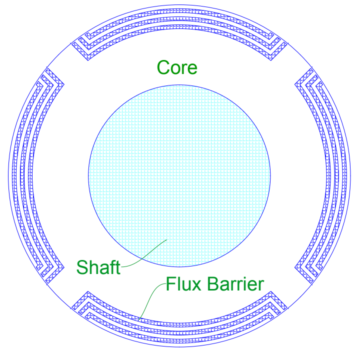

Figure 4.2: Asymmetric flux barrier rotor topology

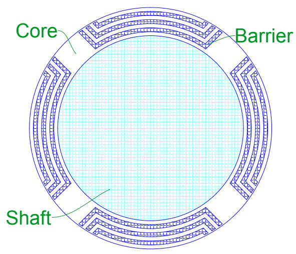

Figure 4.3: Reduced-diameter asymmetric flux barrier rotor topology

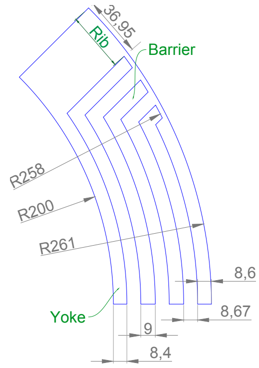

Figure 4.4: Dimensions of rotor structure R1

In Figure 4.4, it is indicated the rotor dimensions of the FMaSynRG-R1. Apart from the distinct proportionality between rotor diameter and total flux-barrier length, the FMaSynRG-R1 differs from the FMaSynRM in the magnet coverage, which is the ratio of the magnet width and the pole pitch. As a result, the circumferential distance between two poles called rib is increased. The selected magnet coverage is 0.73 times the pole pitch τ_p, where the magnet width is measured from the ends of the outer flux barrier. Figure 4.5 shows how to obtain the magnet coverage for this FMaSynRG.

The importance of the magnet coverage lies on the machine efficiency. This ratio affects not only the average torque, but also the iron losses since the tooth eddy currents increase when it is close to one. According to [10] a good magnet coverage should be less than 0.745.

On the other hand, the inner and outer stator diameters are also modified with respect to Table 4.1. A simple rule of three is utilized by taking as a reference the new outer rotor diameter equal to 522 mm. The electromagnetic reasons why the

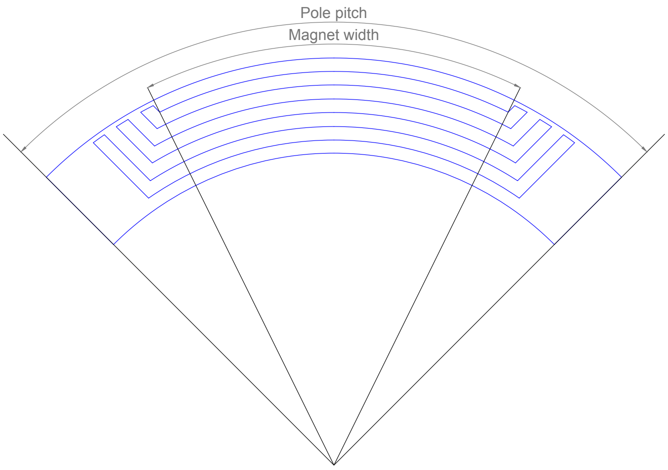

Figure 4.5: Magnet coverage equal to 0.73 in R1

rotor machine is reduced is detailed in section 4.2.

4.1.1.2 Second rotor design approach

The rotor design number 2 (R2) is completely similar to the one in chapter 3 with larger size, whose dimensions are found with a simple rule of three, and are illustrated in Figure 4.6.

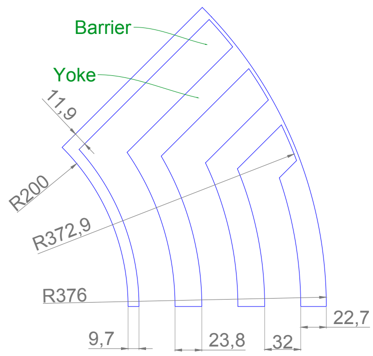

Figure 4.6: Dimensions of rotor structure R2

Due to the size of the flux barriers and the space among them, the resulting magnet coverage is 0.48. Besides, the straight flux barrier rotor topology cannot be drawn, thus only the asymmetric topology is shown.

4.1.2 Main Dimensions

The main dimensions refer to the air-gap length and the equivalent core length. The former is the gap between the stator and the rotor machine, and the latter considers the effects of field fringings and possible ventilation ducts. In both cases, the length is determined based on the machine rated power.

4.1.2.1 Air Gap

The air gap basically defines the machine characteristics, thus a smaller length is endorsed. However, it is subjected to mechanical constraints that are more difficult to endure with larger machines. Additionally, a small air gap brings about higher rotor eddy-current losses, due to its lower permeance. Although the air gap has an important role in the machine performance, there is not a theoretical expression to calculate it. Nevertheless, the empirical Equation 4.1 is employed, which is assigned for induction machines but similar results are attained when the number of pole-pair is greater than 1 [10].

$$g = 0.18 + 0.006P^{0.4} \tag{4.1}$$

where P is the rated power of the machine, in this case 5 MW. Therefore, the air gap equals 3 mm, the outer rotor diameter for R1 is 522 mm, and 752 mm for R2.

4.1.2.2 Equivalent core length

The equivalent core length of this study does not take into account the ventilation ducts, and only considers the field at the edges, where the flux density remains approximately constant for certain length. The flux at the edges decreases gradually to zero along the shaft of the machine, which also contributes in torque production [13]. Figure 4.7 shows the influence of the edge field at the machine end, and Equation 4.2 is an approximation of the equivalent length.

$$\ell' = \ell + 2g \tag{4.2}$$

The produced torque by the rotor can be represented as a function of the tangential stress $\sigma_{F_{tan}}$, the rotor ratio r_r and the equivalent length ℓ' according to [13] as it is detailed in Equation 4.3

$$T = 2\,\pi\, r_r^2\, \ell'\, \sigma_{F_{tan}} \tag{4.3}$$

Without considering the losses and from the given data of Table 4.1, the torque can be found as the ratio between the rated power and the rated speed, thus obtaining 31.83 kNm. On the other hand, Table 4.2 lists the permitted electromagnetic values to design non-salient pole synchronous machines, from which the average stress tangential value is taken. Even though a SynRM works electrically as a salient pole

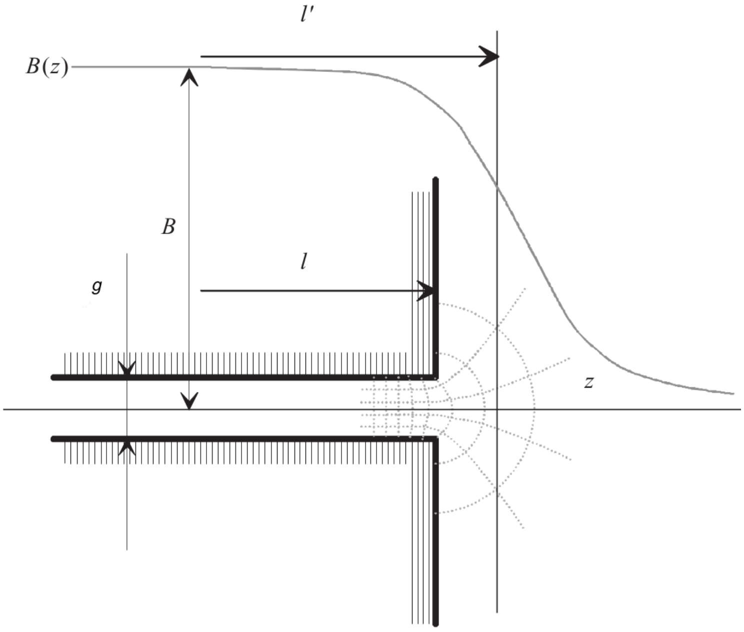

Figure 4.7: Orthogonal field diagram for the determination of the edge field at the end of the machine [13]

Table 4.2: Permitted electromagnetic values for standard non-salient pole synchronous machines with air cooling and spatial phase shift $\zeta = 0$ [13]

Parameter	Value
Air-gap flux density	0.85 - 1.05 T
Stator yoke flux density	1.0 - 1.5 T
Tooth flux density	1.5 - 2.0 T
Armature winding linear current density	30 - 80 kA/m
Minimum tangential stress	17000 Pa
Average tangential stress	36000 Pa
Maximum tangential stress	59500 Pa

synchronous machine, the design is based on mechanical constraints based on the cooling system, hence the non-salient pole data is employed.
Finally, by substituting Equation 4.2 into Equation 4.3 the length of the machine is found as it follows for R1 and R2.

$$\ell_1 = \frac{T}{2\pi\, r_r^2\, \sigma_{F_{tan}}} - 2g = \frac{31.83\, kNm}{2\pi \cdot (0.261\, m)^2 \cdot (36000 Pa)} - 2 \cdot (3\, mm) = 2060\, mm$$

$$\ell_2 = \frac{T}{2\pi\, r_r^2\, \sigma_{F_{tan}}} - 2g = \frac{31.83\, kNm}{2\pi \cdot (0.376\, m)^2 \cdot (36000Pa)} - 2 \cdot (3\, mm) = 989\, mm$$

A brief conclusion can be drawn from these results. The length of R1 is more than twice R2, which represents larger nacelle size in a wind turbine application.

4.1.3 Stator Design

Since there are already some data taken from [10], the design focuses on the physical aspects of the machine such as armature winding and slot dimensions. Additionally, this study takes as a reference the stator geometry detailed in [10], hence the slot heights are kept, and only the circumferential dimensions of the stator are sized. Some parameters like saturation factor and magnetic voltages, can be part of a complementary future job.

4.1.3.1 Winding Selection

The selection of the number of slots depends on how smooth the current waveform must be. In other words, by increasing the number of slots, the winding factor is almost one, thence a more sinusoidal current waveform is attained. However, it increments the number of coils and also the machine cost. Moreover, this selection depends on the cooling system that the system requires. As a hint, small machines have lower slot pitch than big machines. According to [13], the slot pitch τ_u of large PMSM's has to be in between 14 to 75 mm. Table 4.3 sums up the slot-pitch options according the number of slots.

Table 4.3: Slot pitch τ_u with respect to the number of slots $\mathcal{Q}$

q: slots per pole per phase	2	3	4	5	6
$\mathcal{Q} = 2\,\mathfrak{p} \cdot m \cdot q = (2)(2)(3)(q)$	24	36	48	60	72
R1: $\tau_{u_{R1}} = \pi \cdot D_{s_{R1}}/\mathcal{Q} = 522\pi/36$ [mm]	69.12	46.08	34.56	27.65	23.04
R2: $\tau_{u_{R2}} = \pi \cdot D_{s_{R2}}/\mathcal{Q} = 758\pi/36$ [mm]	99.22	66.15	49.61	39.69	33.07

where $\mathcal{Q}$ is the total number of slots, and D_s is the stator inner diameter. It is clear that a stator with 24 slots is close to the upper permitted value equal to 75 mm for a machine with R1, and it is out of the range for R2, so it is not a possible option. As a result, the stator with 36 slots is selected and the other options can be part of a future work.

On the other hand, a full-pitched stator coil configuration is selected, which means the number of slots per pole ($y_{\mathcal{Q}}$) is equal to number of slots spanned by the coil, in this case nine slots

$$W = \frac{9}{9}\tau_p$$

where τ_p is the pole pitch, which is given by Equation 4.4. Then, the winding factor for the fundamental is found with Equation 4.5. Either for R1 or R2, the winding factor is the same.

$$\tau_p = \frac{\pi D_s}{2\mathfrak{p}} \tag{4.4}$$

$$k_{w1} = sin\left(\frac{W\pi}{2\tau_p}\right) \cdot \frac{sin\left(\frac{\pi}{2m}\right)}{q\,sin\left(\frac{\pi}{2mq}\right)} \tag{4.5}$$

$$k_{w1} = 0.9598$$

4.1.3.2 Number of Winding Turns

According to [13], Equation 4.6 allows to find the required number of coil turns in series in a phase winding. However, to continue with the design procedure, some parameters are unknown, thence they are assumed. First, the phase voltage E_m is taken from the analysis done by [10] regarding a PMaSynRM. This value is only a reference for this calculation and will be different from the final model. Then, the arithmetical average coefficient of the flux density of one pole α_i takes a value of 0.75 when a saturation factor k_{sat} is equal to one. This is a good approximation considering in practice α_i does not exceed 0.77 [13]. Next, the air-gap flux density $\hat{B_\delta}$ is taken from the range given by Table 4.2. In such a way, $\hat{B_\delta}$=0.95 T is selected. Finally, the other parameters take the values of the previous calculations.

$$N_\Phi = \frac{\sqrt{2}E_m}{\omega\, k_{w1}\, \ell'\, \tau_p\, \alpha_i\, \hat{B_\delta}} \tag{4.6}$$

$$N_{\Phi_{R1}} = \frac{5.28\,kV}{2\pi(50\,Hz)(0.9598)(2.066\,m)(0.415\,m)(0.75)(0.95\,T)} = 29$$

$$N_{\Phi_{R2}} = \frac{5.28\,kV}{2\pi(50\,Hz)(0.9598)(0.989\,m)(0.595\,m)(0.75)(0.95\,T)} = 42$$

For R1 it is chosen to have in a phase 30 turns in series, which means 60 conductors (each coil comprises 2 conductors), and 42 turns in series in the case of R2, thence 84 conductors. The total number of conductors in a three-phase winding configuration is $2amN_\Phi$, where a represents four parallel paths, similarly to the winding configuration of FMaSynRM. Therefore, the number of conductor per slot is

$$N = \frac{2am}{Q}N_\Phi \tag{4.7}$$

$$N_{_{R1}} = 20\,conductors$$

$$N_{_{R2}} = 28\,conductors$$

4.1.3.3 Tooth Width

The size of the tooth width depends on the dimensions of the slot area, hence this geometry is subjected to changes. However, this width cannot vary too much from its designing value.

$$b_d = \frac{\ell' \, \tau_u}{k_{Fe}(\ell - n_v b_v)} \cdot \frac{\hat{B}_\delta}{\hat{B}_d} + 0.1mm \tag{4.8}$$

Equation 4.8 allows to find the tooth width, where k_{Fe} is the space factor of iron and it assumed to be 0.97. $n_v b_v$ represents the sum of the ventilation ducts that are neglected, and $\hat{B}_d$ is the permitted flux magnetic density in the tooth. The latter is taken from Table 4.2 and equals 1.75 T. Subsequently,

$$b_{d_{R1}} = \frac{(2.066\,m)(0.04608\,m)}{0.97(2.060\,m)} \cdot \frac{0.95\,T}{1.75\,T} + 0.1\,mm = 26\,mm$$

$$b_{d_{R2}} = \frac{(0.989\,m)(0.06615\,m)}{0.97(0.989\,m)} \cdot \frac{0.95\,T}{1.75\,T} + 0.1\,mm = 37\,mm$$

4.1.3.4 Slot Dimensions

The final step is to deduce the slot area for the required conductors. A fill factor k_f equal to 0.45 is chosen, which is the maximum coefficient suggested by [13] for large machines and rectangular wires. It is assumed that a current density of 4.4 A/mm^2 brings about the rated power, with the phase current equals 315 A$_{rms}$ for R1 and 442 A$_{rms}$ for R2, then their peak values are found.

$$I_{peak_{R1}} = 630A \cdot \sqrt{2} = 890.95\;A$$

At this point, the design has a small modification, since only two parallel paths (a = 2) are considered, but the number of conductors per slot is kept. This is done in order to increase the slot area, then the conductor cross-sectional area is calculated.

$$S_c = \frac{I_{peak}}{aJ_{peak}} \tag{4.9}$$

$$S_{c_{R1}} = 50.62\,mm^2$$

$$S_{c_{R2}} = 71.03\,mm^2$$

Next, the slot cross-sectional area is found by multiplying the number of conductor per slot times the conductor cross-sectional area, and divided by the fill factor.

$$S_{slot} = \frac{N\,S_c}{k_f} \tag{4.10}$$

$$S_{slot_{R1}} = 2250\,mm^2$$

$$S_{slot_{R2}} = 4420\, mm^2$$

Finally, the slot geometry can be approximated to a trapezoid in order to determine the upper and bottom sides. The slot height keeps the proportionality from [10], and also the ratio between the two bases is kept.

$$\frac{b_2}{b_1} = \frac{3}{2}$$

$$S_{slot} = \frac{(b_1 + b_2)h}{2}$$

Table 4.4: Calculated values of b1 and b2

Parameter	R1	R2
b_1	27.5 mm	37.6 mm
b_2	41.2 mm	56.4 mm

The above are adjusted until a symmetrical structure is obtained. The slot geometries are illustrated in Figure 4.8 and Figure 4.9 for R1 and R2 respectivily.
The final dimensions of the complete designs are listed in Table 4.5 and Table 4.6.

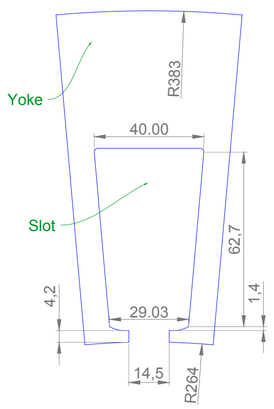

Figure 4.8: Slot dimensions of stator for R1

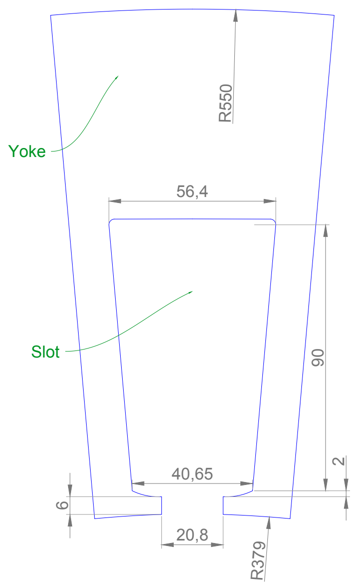

Figure 4.9: Slot dimensions of stator for R2

Table 4.5: Summary of main dimensions of FMaSynRG with rotor R1

Parameter	Value
Air gap	3 mm
Core length	2060 mm
Number of slots	36
Number of conductors per slot	20
Stator inner diameter	528 mm
Stator outer diameter	766 mm
Slot base b_1	29.03 mm
Slot base b_2	40.00 mm
Rotor inner diameter	400 mm
Rotor outer diameter	522 mm
Magnet coverage	0.73
Rotor rib	36.95 mm

Table 4.6: Summary of main dimensions of FMaSynRG with rotor R2

Parameter	Value
Air gap	3 mm
Core length	989 mm
Number of slots	36
Number of conductors per slot	28
Stator inner diameter	758 mm
Stator outer diameter	1100 mm
Slot base b_1	40.65 mm
Slot base b_2	56.4 mm
Rotor inner diameter	400 mm
Rotor outer diameter	752 mm
Magnet coverage	0.48
Rotor rib	16 mm

4.2 Results of Electromagnetic Parameters

Once again the electromagnetic parameters are calculated by employing the finite element method, as it was done in section 3.4. Also, either for R1 and R2, a Halbach

array is employed to identify the magnetization direction of the small elements that compose each flux barrier; consequently, a air-gap magnetic flux is attained.
As first analysis, the magnetic flux density without stator currents is compared between the two models. In Figure 4.10 and Figure 4.11 the green surface represents the tooth and the purple one the slot. On the left of the tooth, the air gap presents a blue color, which in the flux density scale indicates a magnitude around 0.25 T for R1 and 0.33 T for R2. The difference lies on the less ferrite magnet used in R1, due to the smaller rotor size and flux barrier thickness. The reason of this smaller rotor design is because of the unused core material as it is depicted in Figure 4.12, where the magnetic flux lines do not cover a vast rotor yoke volume. Subsequently, the size of the machine is decrease, thence saving unused material.

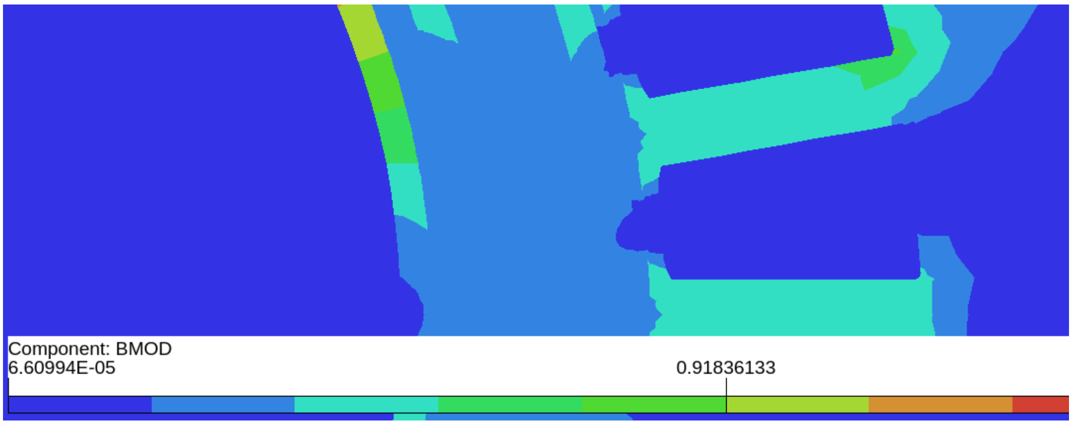

Figure 4.10: Air-gap flux density of the FMaSynRG with rotor R1

Figure 4.11: Air-gap flux density of the FMaSynRG with rotor R2

The calculation of the electromagnetic parameters follows the described procedure done for the FMaSynRM in section 3.4, hence only the results are analyzed in this chapter.

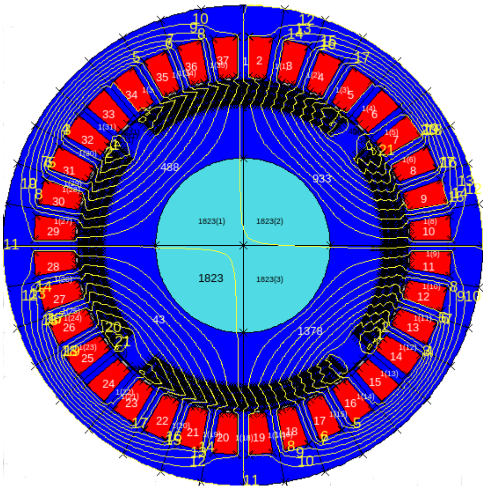

Figure 4.12: Initial size of FMaSynRG with R1

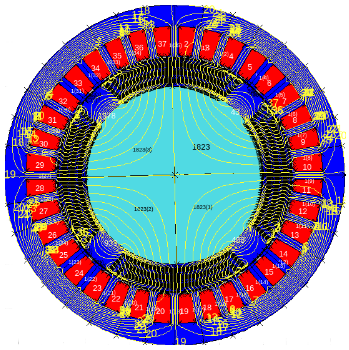

Figure 4.13: Final size of FMaSynRG with R1

4.2.1 Magnetic Flux

The coil arrangement per phase in the FMaSynRG, illustarted in Figure 4.14, is different from the one in subsection 3.2.2. Since each slot-pair houses one coil, the equivalent coil is represented by only one inductor. Additionally, the 36 slots are distributed in six slots per phase per pole-pair, where three windings are housed and connected in series. Then, the magnetic flux per phase is the sum of the flux in each coil connected in series, since these two set of windings per pole-pair are connected in parallel.

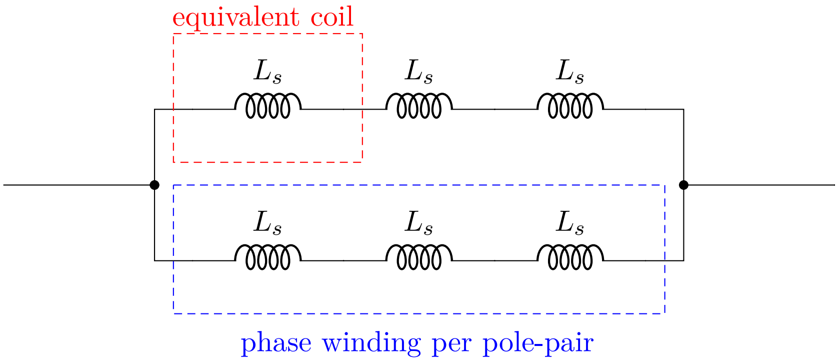

Figure 4.14: Coil arrangement per phase in FMaSynRG

The resultant flux waveforms for the FMaSynRG with rotor R1 and R2 are shown in Figure 4.15 and Figure 4.16 respectively. Even though the magnetic flux in R2 has a peak value higher than R1, the waveform is not so smooth, hence more harmonic distortion is seen. This is because of the low magnet coverage. In the case of R1, the circular arc covered by the radial flux barriers is greater than the circumferential flux barriers. In Figure 4.17 it can be seen that six slots are covered by the width of the radial flux barrier, and only one by the thickness of the circumferential flux barriers. On the other hand, Figure 4.18 shows that four slots are covered by the radial flux barrier and two and a half by the circumferential ones.

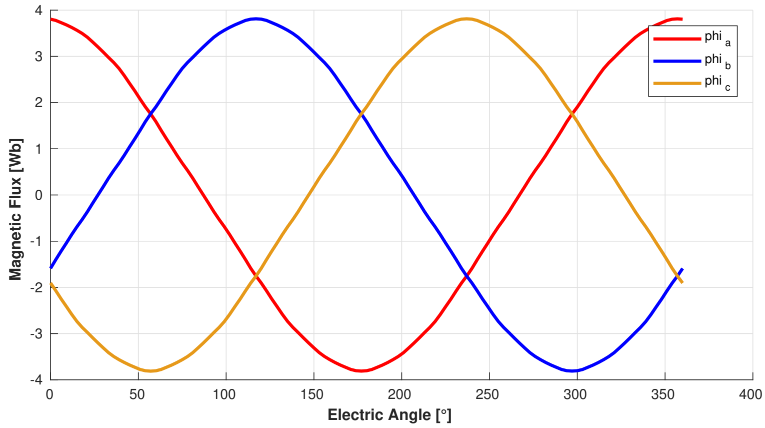

Figure 4.15: Induced magnetic flux in the stator windings of the FMaSynRG with R1

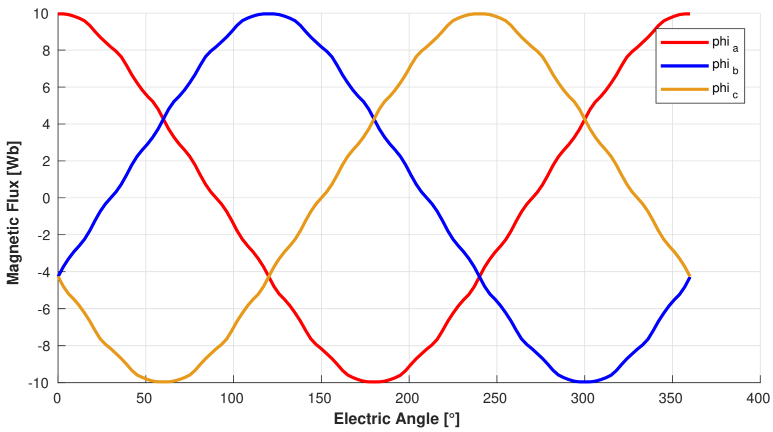

Figure 4.16: Induced magnetic flux in the stator windings of the FMaSynRG with R2

4.2.2 Torque

The torque waveforms for a blocked-rotor test are depicted in Figure 4.19 and Figure 4.20 for R1 and R2 respectively. The mismatch is due to the calculation method. The torque calculation in regions 1 to 5 considers the air gap itself, while the torque equation takes the magnetic flux and current values in the windings.

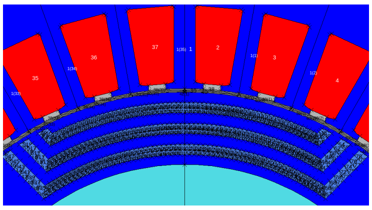

Figure 4.17: Magnet coverage for R1

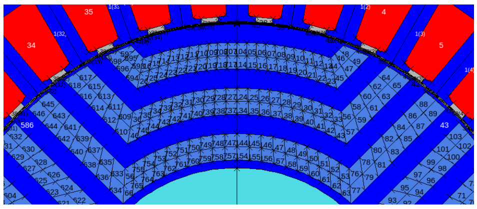

Figure 4.18: Magnet coverage for R2

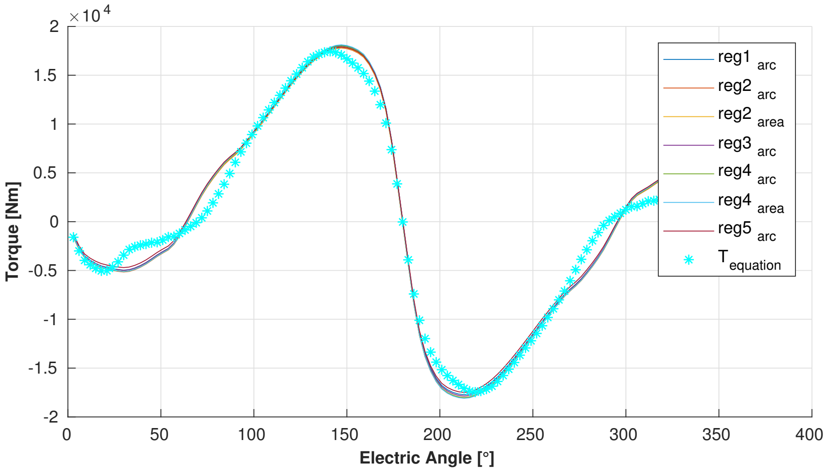

Figure 4.19: Torque waveform with blocked rotor and 4.4 A/mm^2 for R1

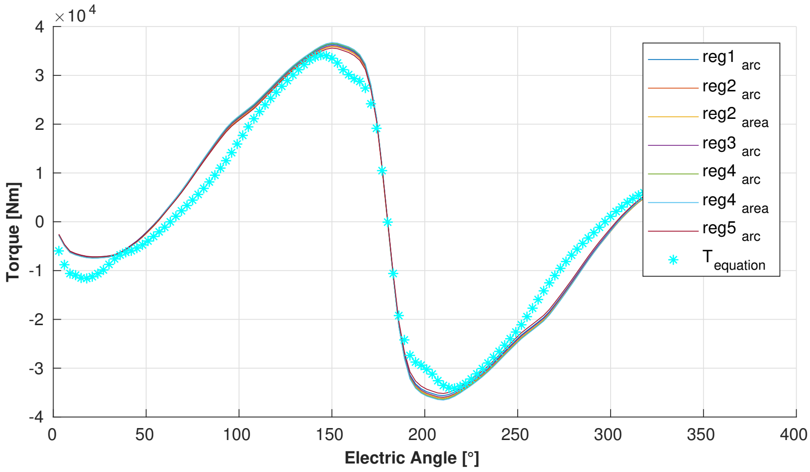

Figure 4.20: Torque waveform with blocked rotor and 4.4 A/mm^2 for R2

Even though the injected current in the simulation is a smooth sinusoidal waveform, the induced flux is not because of the geometry of the machine. In other words, the slot openings and the flux barriers bring about a distorted magnetic flux waveform.

In Table 4.1 was mentioned that the nominal angular speed is equal to 1500 rpm (50π rad/s), thus the length or the angular speed of the FMaSynRG with R1 should be increased in order to reach this torque. In the case of R2, the nominal torque is easily attained at nominal angular speed.

4.2.3 Inductance in dq frame

Another parameter to analyze is the inductance in the dq-frame. Figure 4.21 and Figure 4.22 show the inductances in the d- and q-axes with respect to the phase current for R1 and R2 respectively. In both cases, the tendency is similar, but the values differ somewhat. With a current density of 4.4 A/mm^2, the phase current and inductance are listed in Table 4.7.

Table 4.7: Results with a current density of 4.4 A/mm^2

Structure	**Phase Current** [A]	$\mathbf{L}_d$ [mH]	$\mathbf{L}_q$ [mH]	$\mathbf{L}_q$-$\mathbf{L}_d$ [mH]	$\mathbf{L}_q/\mathbf{L}_d$
R1	445.8 A	12.10	26.86	14.76	2.2
R2	642.9 A	12.57	37.52	24.95	3.0

From the previous results the low salient ratio is responsible for the low reluctance torque. However, in the case of R2 the product of the difference between the inductances ($L_d - L_q$), and the phase current are high enough to produce a even higher reluctance torque that the IPMSG given in [10]. These results are listed and compare in Table 4.8.

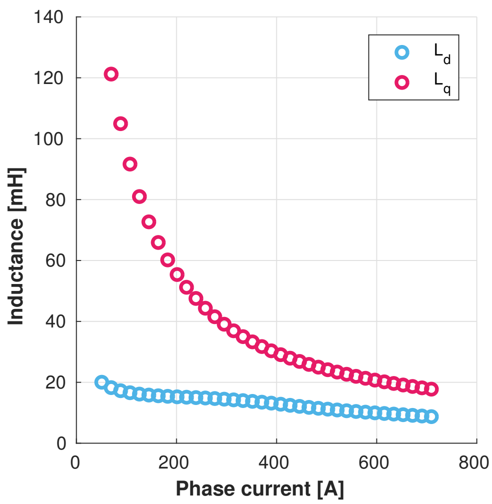

Figure 4.21: Inductances for R1

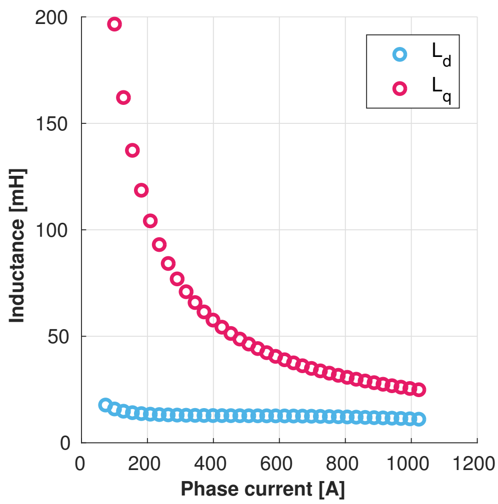

Figure 4.22: Inductances for R2

Table 4.8: Torque with current density equal to 4.4 A/mm^2

Parameter	FMaSynRG-R1	FMaSynRG-R2	IPMSG [10]
Average Torque	-17.15 kNm	-33.77 kNm	-64.60 kNm
Reluctance Torque	-11.59 kNm	-21.96 kNm	-19.50 kNm
Angular Speed	1500 rpm	1500 rpm	750 rpm
Pole-pair	2	2	4

4.2.4 Back-EMF

The back-electromotive force (back-EMF) can be calculated by taking the magnetic flux and the rotor electrical angular speed, as it is depicted in the Equation 4.11 and Equation 4.12.

$$e_d = -\omega_r \lambda_q \tag{4.11}$$

$$e_q = \omega_r \lambda_d \tag{4.12}$$

where the phase peak back-EMF is found

$$e_{\phi,peak1} = \omega_r \sqrt{\lambda_d^2 + \lambda_q^2} \tag{4.13}$$

Additionally, the back-EMF can be found by using the Fadaray's law of induction detailed in subsection 2.1.1. Nevertheless, a modification of this expression is employed as it is done by [25]. Subsequently, the back-EMF results from the ratio between the magnetic flux and the angular electrical position times the rotor electrical angular speed.

$$e_{\phi,peak2} = -\frac{d\lambda}{dt} = -\omega_r \frac{\Delta\lambda}{\Delta\theta_r} \tag{4.14}$$

The results of these two method are listed in Table 4.9, which present a small error that is negligible in the case of R2.

Table 4.9: Peak phase voltage of the FMaSynRG's when $\omega_m = 50\pi$ rad/s

Structure	λ_d [Wb]	λ_q [Wb]	$e_{\phi,peak1}$ [V]	$e_{\phi,peak2}$ [V]
R1	2.01	20.00	6314.84	6441.07
R2	2.84	21.86	6925.32	6923.22

Even though R1 uses less ferrite magnet, the induced magnetic flux is similar than R2 due to its longer length, thence comparable back-EMF. Besides, despite the reduced harmonic component on the induced magnetic flux in R1, the electromagnetic torque does not fulfill the requirement for a 5-MW FMaSynRG. At this point, it is clear that the rotor design R2 provides better results to be worthy of comparison with the ones in [10] as it is detailed in Table 4.10. Therefore the R1 design is considered no longer in this report.

Table 4.10: Comparison analysis between FMaSynRG's and IPMSM

Parameter	FMaSynRG-R1	FMaSynRG-R2	IPMSG
Reluctance Torque	-11.59 kNm	-21.76 kNm	-19.50 kNm
Peak Phase Current	445.8 A	642.9 A	784.9 A
Peak Back-EMF	6.31 kV	6.92 kV	5.04 kV

4.2.5 Power Factor

Figure 4.20 shows that the peak torque is reached when the current space vector is leading 150° the d-axis, when a current density of 4.4 A/mm^2 is injected in the stator windings. In the case of a generator, the sign of the second term of torque equation 2.54 changes due to the opposite current direction, as it is illustrated in Figure 4.23 and Figure 4.24.

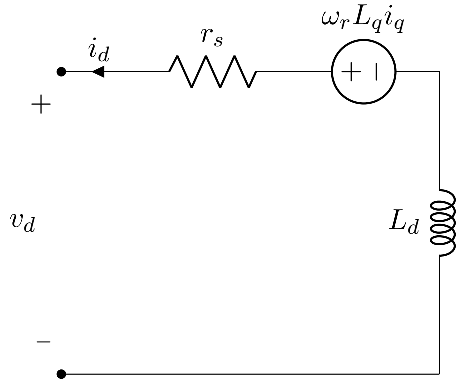

Figure 4.23: Equivalent circuit in the d-axis for a generator

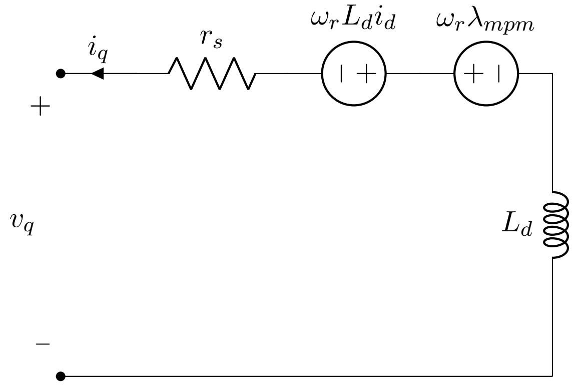

Figure 4.24: Equivalent circuit in the q-axis for a generator

Therefore, the torque can be found by Equation 4.15.

$$T_e = \frac{3}{2}\mathfrak{p}(\lambda_{mpm} i_q - (L_d - L_q) i_q i_d) \tag{4.15}$$

Since L_q is greater than L_d, i_d has to be positive in order to participate in torque generation. Hence, the current space vector and the d-axis form an angle of 30°.

Under this conditions and based on the collected data, the power factor equal to 0.79 is found and detailed in Appendix C. This outcome has a considerable improvement if it is compared with the case of a reluctance machine without ferrite magnets, where power factor basically depends on the salient ratio.

$$cos(\phi) = \frac{L_q - L_d}{L_q + L_d} = \frac{37.52 - 12.57}{37.52 + 12.57} = 0.5$$

The reason of this enhancement lies on the increased back-EMF due to the ferrite magnet flux. The latter compensates the lagging angle caused by the inductance component.

4.3 Generated Power and Efficiency

The selected FMaSynRG ideally ($P_{in} = P_{out}$) is able to generate just about 5 MW when the current density in the stator windings is equal to 4.4 A/mm^2. This means that the required output power is reached at a lower current density, in comparison with the IPMSG. However, this rough output power is lower when the losses are considered. Hereafter, the copper and iron losses in the FMaSynRG are calculated, and based on these results the efficiency is found.

4.3.1 Copper Losses

The copper losses depend on the current and electrical resistance of the coils. To find the latter, the resistivity, cross-sectional area and length of the conductor are needed. The copper resistivity coefficient at 20°C equal to 1.724·10^{-8} Ωm is taken since it does not vary so much when the temperature is increased. The calculation of the conductor cross-sectional area draws from the slot cross-sectional area, by knowing that 45% of this surface is covered by 28 conductors.

$$S_c = \frac{k_f \cdot S_{slot}}{n_c}$$

where S_c and S_{slot} are the conductor and slot cross-sectional areas respectively, k_f the fill factor, and n_c the number of conductor in one slot.

$$S_c = \frac{0.45 \cdot 4545.61\, mm^2}{28} = 73.05\, mm^2$$

Next, the length of the coil is divided in three sections. The one housed by the slot is equal to the length of the machine ℓ. The second one takes the circle arc of the pole pitch plus some extra length ℓ_k to complete the loop.

$$\tau_{p,c} = \frac{\pi \cdot D_c}{2\mathfrak{p}}$$

where $\tau_{p,c}$ is the circle arc covered by the conductor, D_c the diameter of a circle whose origin is in the shaft and its ratio ends in the middle of a slot.

$$\tau_{p,c} = \frac{\pi \cdot 0.986\, m}{4} = 0.774\, m$$

then,

$$\ell_c = \ell + \tau_{p,c} + \ell_k$$
$$\ell_c = 0.989\, m + 0.774\, m + 0.25\, m = 1.024\, m$$

In order to calculate the conductor resistance of the three coils connected in series r_{branch} of Figure 4.14, the Equation 4.16 is used, whose variables has been defined above. The resulting resistance is multiply by 28 conductors per slot and 6 slots per pole-pair.

$$r = \rho \frac{\ell}{S_c} \tag{4.16}$$

$$r_{branch} = (6)(28)(1.724 \cdot 10^{-8}\ \Omega m)\, \frac{1.024\, m}{7.305 \cdot 10{-}5\, m^2} = 79.82\, m\Omega$$

as two branches are connected in parallel, the equivalent conductor resistance per phase is

$$r_s = 39.91\, m\Omega$$

finally, the copper losses are found by

$$P_{cu} = 3\, {I_{rms}}^2\, r_s \tag{4.17}$$

where $I_{rms} = 642.9/\sqrt{2}\, A$, and 3 represents the number of phases.

$$P_{cu} = 24.74\, kW$$

4.3.2 Iron Losses

To determine the iron losses, the magnetic flux densities in the stator and rotor yoke are calculated by OperaFEA. First, the slot core cross-sectional area is divided in three sections, as it is shown in Figure 4.25, where the flux densities in the x- and y-axes are calculated. Subsequently, the resulting magnitude from these two coordinates is multiply by the corresponding core-loss density detailed in Appendix A to find the equivalent power loss. Likewise, the rotor iron losses are obtained by following the same procedure, except that only one point is considered as it is depicted in Figure 4.26. Table 4.11 sums up the iron loss in these four sections.

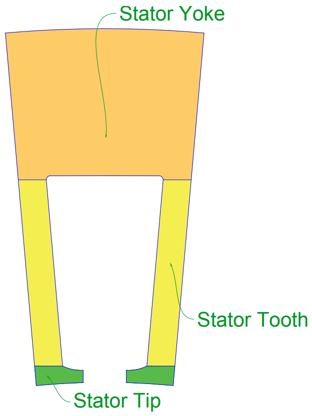

Figure 4.25: Stator sections and points where B_x and B_y are calculated

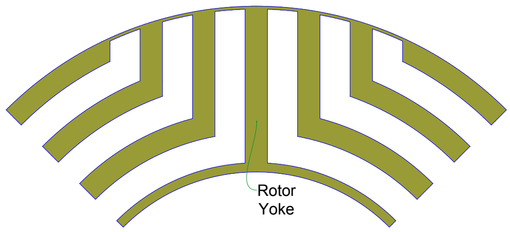

Figure 4.26: Rotor section and point where B_x and B_y are calculated

Section	Core Loss [W]
Stator Tip	277.87
Stator Tooth	2666.75
Stator Yoke	5864.15
Rotor Yoke	4776.75
Total Iron Losses	13585.52

Table 4.11: Iron losses in the FMaSynRG

4.3.3 Efficiency

The efficiency of the FMaSynRG results from the ratio between the output power and the sum of the output power, copper and iron losses. From Equation 4.18 the efficiency is found.

$$\eta = \frac{P_{out}}{P_{out} + P_{cu} + P_{fe}} \cdot 100\% \tag{4.18}$$

$$\eta = \frac{5000\,kW}{5000\,kW + 24.74\,kW + 13.59\,kW} = 99.24\%$$

It is worth mentioning that mechanical losses are not considered and are not part of this project; consequently, the actual efficiency is lower.

4.4 Active material weight

The active material weight of the FMaSynRG is compared with the IPMSG from [10]. The results are listed in Table 4.12. However, the permanent and ferrite magnet weight are not considered.

Table 4.12: Active material weight

Parameter	IPMSG	FMaSynRG
Stator core steel weight	2397 kg	2504 kg
Rotor core steel weight	1815 kg	1078 kg
Copper weight	1024 kg	1328 kg
Total active material weight	5236 kg	4910 kg

Since the FMaSynRG has 36 slots, there is more core material. However, the used iron in the rotor is less due to the flux barrier size. Although there is no data, the permanent magnets of the IPMSG have larger density than the ferrite ones, thence more active material weight than the FMaSynRG.

Chapter 5

FMaSynRG Control System

In this chapter, the performance of the designed FMaSynRG is tested by using MatLab in a generation system model. The later consists basically in a wind turbine, the mathematical model of the FMaSynRG and two PI controllers. To make the analysis easier, an constant angular mechanical speed is settled. Therefore, these three MatLab blocks are detailed hereafter whose results are also shown.

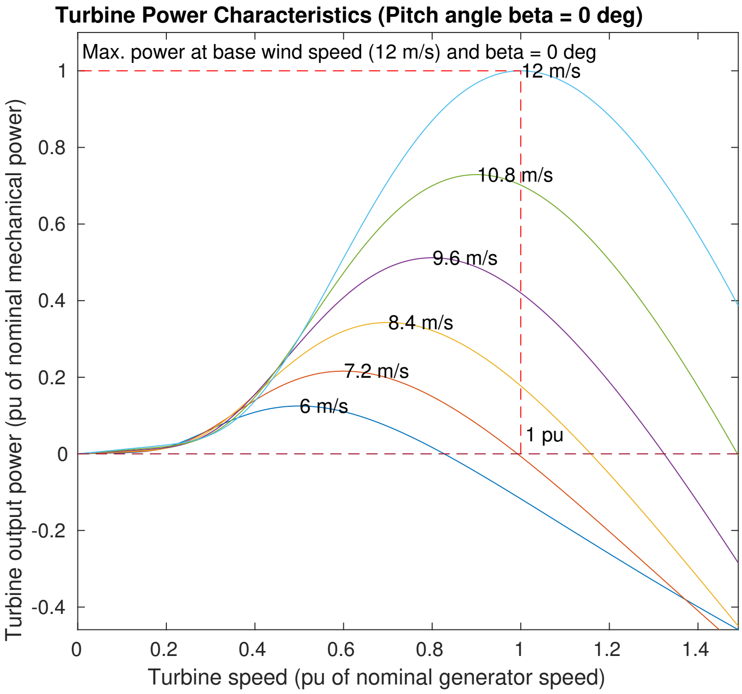

Figure 5.1: Turbine output power vs Turbine speed [27]

5.1 Wind Turbine Model

The wind turbine MatLab model is configured in such a way that the maximum mechanical output power is reached when the wind speed is equal to 12 m/s. The mechanical power as a function of generator speed, for different wind speeds and blade pitch angle β equal to zero is illustrated in Figure 5.1. Subsequently, the resulting mechanical torque is taken. The system schematic is illustrated in Figure 5.2

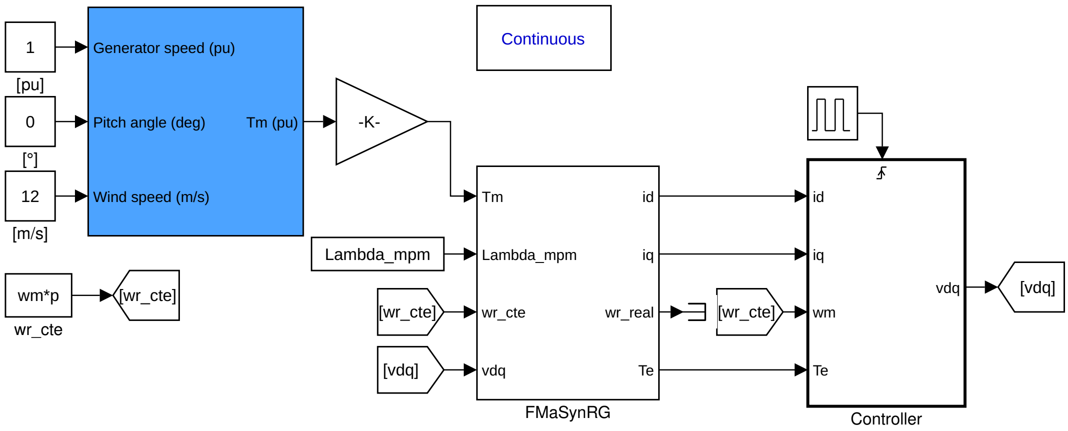

Figure 5.2: General schematic of the FMaSynRG control system

5.2 FMaSynRG Mathematical Model

The mathematical model draws from the expressions of section 2.5. However, since the machine works as a generator, the current direction is changed, resulting in Equation 5.5 and Equation 5.6.

$$v_d = -r_s i_d - \omega_r \lambda_q + \frac{d}{dt}(\lambda_d) \tag{5.1}$$

$$v_q = -r_s i_q + \omega_r \lambda_d + \frac{d}{dt}(\lambda_q) \tag{5.2}$$

$$\lambda_d = -L_d i_d + \lambda_{mpm} \tag{5.3}$$

$$\lambda_q = -L_q i_q \tag{5.4}$$

$$v_d = -r_s i_d + \omega_r L_q i_q - L_d \frac{di_d}{dt} \tag{5.5}$$

$$v_q = -r_s i_q - \omega_r L_d i_d + \omega_r \lambda_{mpm} - L_q \frac{di_q}{dt} \tag{5.6}$$

Then, the equivalent circuits in d and q-axes are presented in Figure 5.3 and Figure 5.4

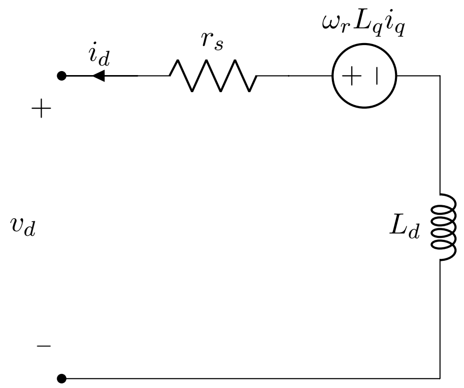

Figure 5.3: Simplified d-axis circuit

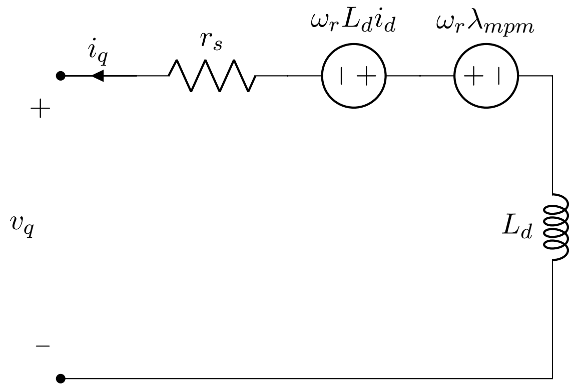

Figure 5.4: Simplified q-axis circuit

Additionally, the electromagnetic torque produced by the FMaSynRG has a small difference. The negative sign of the second term in Equation 5.7 is because of the positive d-axis component of the current vector, since the machine works as a generator. This second term becomes positive due to the fact that the inductance in the q-axis is grater than the one in the d-axis, as it was already demonstrated.

$$T_e = \frac{3}{2}\mathfrak{p}(\lambda_{mpm} i_q - (L_d - L_q) i_q i_d) \tag{5.7}$$

Furthermore, the rotor angular electrical speed can be represented by motion Equation 5.8.

$$J\frac{d\omega_r}{dt} = \mathfrak{p}(T_e - T_m) \tag{5.8}$$

However, this expression is not utilized due to assuming constant rotor angular speed. For dynamic simulation of FMaSynRG equations 5.5 and 5.6 are rearranged

$$i_d = \frac{1}{s}(-v_d - r_s i_s + \omega_r L_q i_q)/L_d \tag{5.9}$$

$$i_q = \frac{1}{s}(-v_q - r_s i_s - \omega_r L_d i_d + \omega_r \lambda_{mpm})/L_q \tag{5.10}$$

After determining the equations of the dynamic model, the block diagram is derived and depicted in Figure 5.5, where the input variables are the dq-axis stator voltages v_d and v_q, the peak flux linkage λ_{mpm}, and the mechanical torque T_m. On the other hand, the output variables are the dq-axis currents i_d and i_q, the rotor electrical angular speed ω_r and the electromagnetic torque T_e.

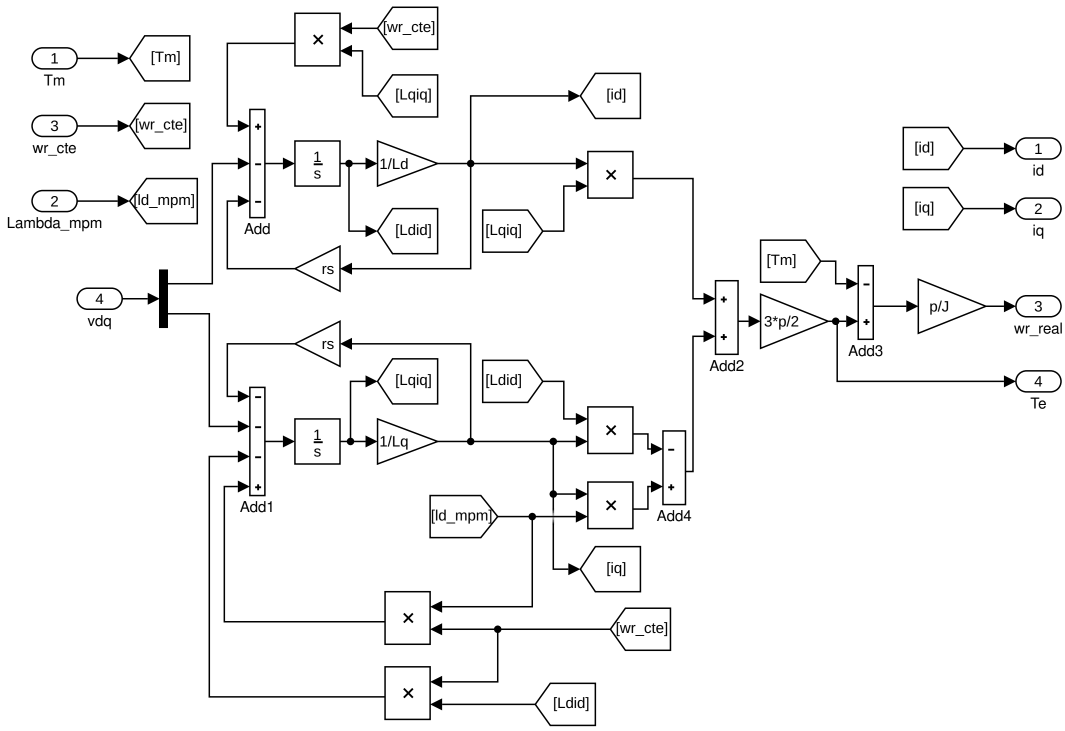

Figure 5.5: Block diagram for dynamic simulation of FMaSynRG

5.3 Controller Design

Before establishing the control method, the transfer function of the machine is required. Equations 5.9 and 5.10 give guidelines to find the transfer functions in d- and q-axes. However, the coupling items between d- and q-axis voltage equations make the analysis more complicated. Figures 5.6 and 5.7 represent the closed-loop block diagrams for i_d and i_q respectively. In both cases, the coupling items are

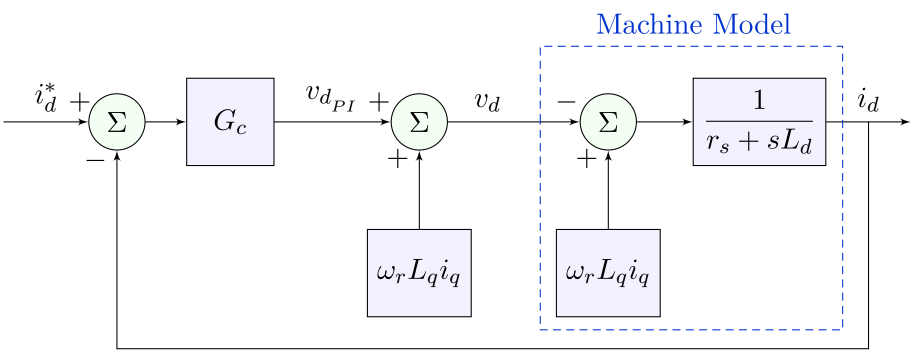

Figure 5.6: Back-EMF decoupling in closed loop for d-axis current

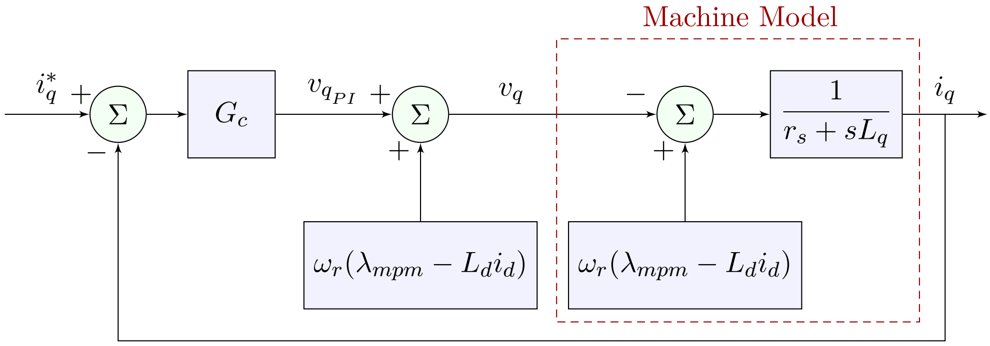

Figure 5.7: Back-EMF decoupling in closed loop for q-axis current

added to the voltage that is applied to the machine. As a result, these two values are subtracted and the equivalent transfer function is defined by a RL-filter. Then, the feedback controller is design without taking into account the back-EMF term [28]. The parameter values are listed in Table 5.1.

Table 5.1: FMaSynRG parameters

Symbol	Meaning	Value
f_1	Grid frequency	50 Hz
f_s	Sampling frequency	10 kHz
L_d	d-axis Inductance	12.57 mH
L_q	q-axis Inductance	37.52 mH
r_s	Phase resistance	39.91 mΩ

The transfer function expressed in Equation 5.11 represents a stable first-order system, where x refers to d- and q-axis inductance. As it can be deducted, the system has no poles on the right hand plane (RHP) and this can be seen in the bode plots of Figure 5.8 and Figure 5.9, where the phase diagrams do not have $-180°$ crossings.

$$G_p = \frac{1}{r_s + sL_x} \tag{5.11}$$

However, to design a controller, a DSP is required. As a result, an additional block after the controller has to be considered. This block represents the computation and PWM delays, and it is depicted in Equation 5.12.

$$G_d = e^{-1.5sT_s} \tag{5.12}$$

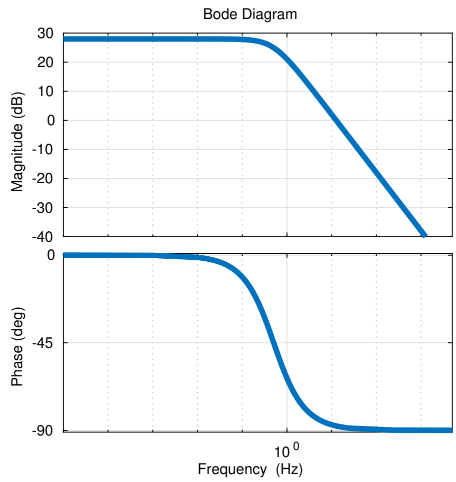

Figure 5.8: Bode plot of d-axis transfer function

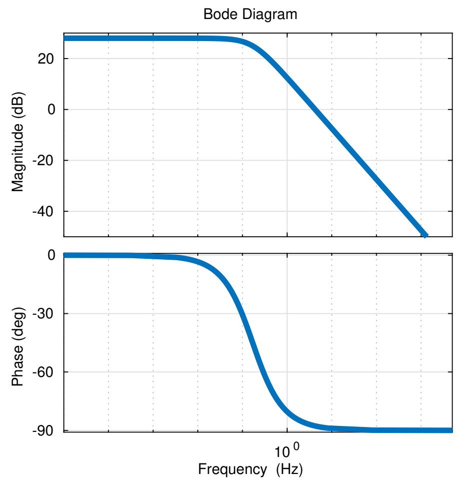

Figure 5.9: Bode plot of q-axis transfer function

where T_s is the sampling period. Figure 5.10 and Figure 5.11 show the impact of the delay on the system. The bode plots have a -180° crossing that brings about a couple of poles on the RHP.

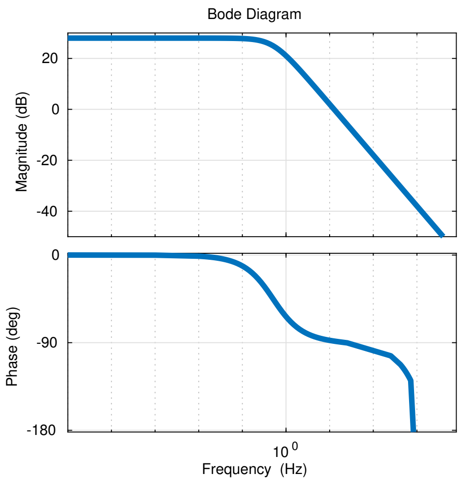

Figure 5.10: Bode plot of d-axis transfer function times the delay G_d

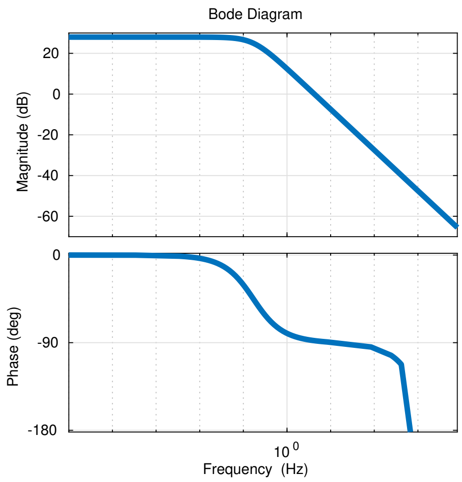

Figure 5.11: Bode plot of q-axis transfer function times the delay G_d

Therefore, the general system control loop is illustrated in Figure 5.12.

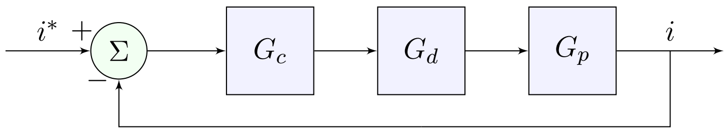

Figure 5.12: Control Loop

5.3.1 PI Controller

Once the characteristics of the plant, a PI controller is chosen (Equation 5.13).

$$G_c = Kp\left(1 + \frac{1}{s\tau_i}\right) = K_p + \frac{K_i}{s} \tag{5.13}$$

To determine the controller gains K_p and K_i, a recommended phase margin value ($\phi_m = \pi/4$ rad) is replaced in the phase angle expression when the frequency is equal to the crossover frequency ω_c.

$$\begin{aligned}\angle G_c(j\omega_c)G_d(j\omega_c)G_p(j\omega_c) &= \angle\frac{K_p}{r_s}\frac{(1 + j\omega_c\tau_i)e^{-j1.5\omega_c T_s}}{j\omega_c(1 + j\omega_c\dfrac{L_x}{r_s})} = -\pi + \phi_m \\ &= Arctan(\omega_c\tau_i) - \pi/2 - 1.5\omega_c T_s - Arctan(1.5\omega_c L_x/r_s)\end{aligned}$$

The cross over frequency ω_c will be above the plant pole frequency, thus $Arctan(1.5\omega_c L_x/r_s)$ will be around $\pi/2$ [29]. Additionally, the maximum value of ω_c for a given ϕ_m occurs when $Arctan(\omega_c\tau_i) = \pi/2$ [29].

$$\phi_m \approx Arctan(\omega_c\tau_i) - 1.5\omega_c T_s$$

$$\omega_{c(max)} = \frac{\pi/2 - \phi_m}{1.5T_s} \tag{5.14}$$

Now, by replacing Equation 5.14 in the gain expression, the value of K_p can be found. Usually $\omega_{c(max)}\tau_i >> 1$ and $\omega_{c(max)}\frac{L_x}{r_s} >> 1$. On the other hand, it was mentioned that $\omega_c\tau_i$ has to be large enough to obtain $Arctan(\omega_c\tau_i) \approx \pi/2$. If instead of $\pi/2$ rad an angle equal to $17\pi/36$ rad is selected, K_i can be found as it shown in Equation 5.16 [29].

$$K_p = r_s\tau_i\omega_{c(max)}\sqrt{\frac{1 + \omega^2_{c(max)}\dfrac{L_x}{r_s}}{1 + \omega^2_{c(max)}\tau_i^2}}$$

$$K_p \approx \omega_{c(max)} L_x \tag{5.15}$$

$$\tau_i = \frac{10}{\omega_{c(max)}} = \frac{K_p}{K_i}$$

$$K_i = \frac{K_p \omega_{c(max)}}{10} \tag{5.16}$$

The implemented PI controllers for the i_d and i_q are shown in Figure 5.13, and the controller parameters are listed in Table 5.2.

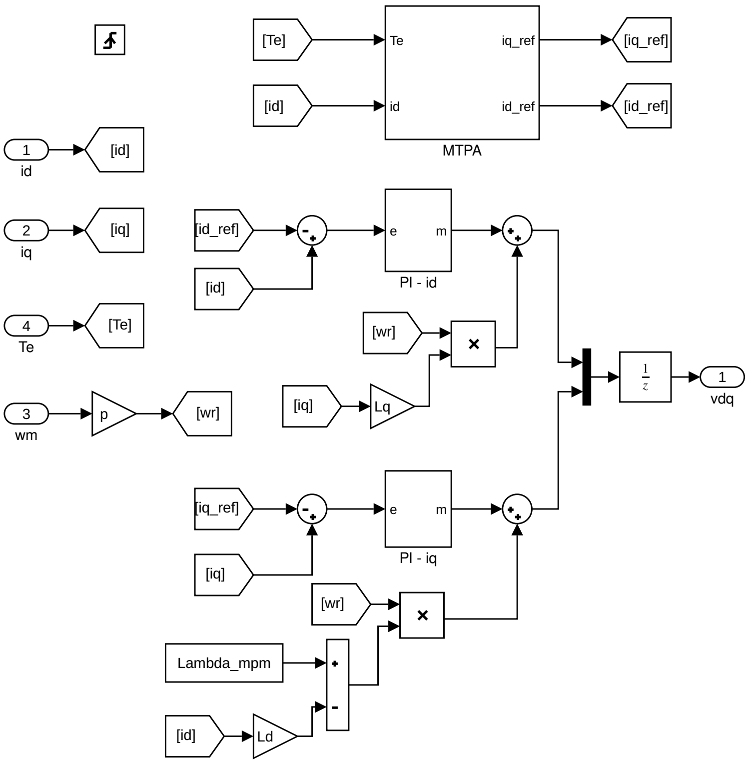

Figure 5.13: PI controller for the FMaSynRG

Finally, the open-loop bode plots of block diagram of Figure 5.12 are shown in Figure 5.14 and Figure 5.15. Furthermore, the resulting gain and phase margin are detailed in Table 5.3.

Table 5.2: Designing controller parameters

Symbol	Meaning	Value
T_s	Sampling period	100 μs
ϕ_m	Phase margin	$\pi/4$ rad
$f_{c(max)}$	Crossover frequency	5.2 kHz
τ_i	Integral time	1.9 ms
$K_{p,d}$	Proportional gain	65.82
$K_{i,d}$	Integral gain	34461.4
$K_{p,q}$	Proportional gain	196.45
$K_{i,q}$	Integral gain	102863.2

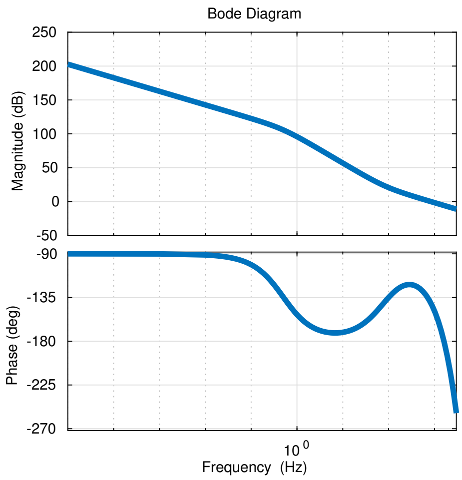

Figure 5.14: Bode plot of d-axis transfer function times the delay G_d and Controller

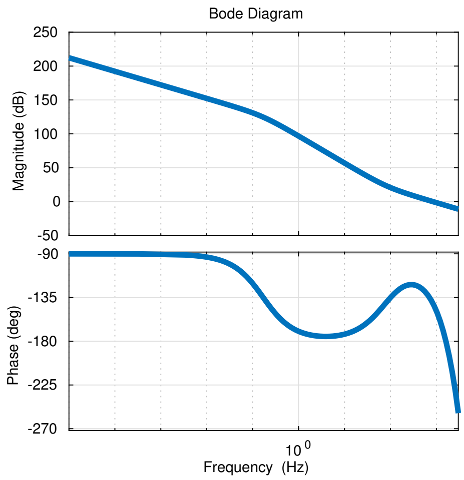

Figure 5.15: Bode plot of q-axis transfer function times the delay G_d and Controller

Table 5.3: Resulting gain and phase margins

Symbol	Meaning	Value
ϕ_m	Phase margin	39.1°
GM	Gain margin	5.72

5.3.2 Maximum Torque Per Ampere

The maximum torque per ampere control generates a given torque with a minimum stator current [30], [31]. To achieve the minimum producing-torque stator current, i_d and i_q are adjusted [32]. For a given current vector i_s, the magnitude of i_d can be found by Equation 5.17.

$$i_d = \sqrt{i_s^2 - i_q^2} \tag{5.17}$$

Substituting the previous equation into Equation 5.7, the electromagnetic torque is expressed as a function of i_q.

$$T_e = \frac{3}{2}\mathfrak{p}(\lambda_{mpm} i_q - (L_d - L_q) i_q \sqrt{i_s^2 - i_q^2}) \tag{5.18}$$

By differentiating Equation 5.18 with respect to i_q

$$\frac{dT_e}{di_q} = \frac{3}{2}\mathfrak{p}\left(\lambda mpm - (L_d - L_q) i_d + (L_d - L_q) i_q^2 \frac{1}{\sqrt{i_s^2 - i_q^2}}\right) = 0 \tag{5.19}$$

then,

$$i_d = \frac{\lambda_{mpm}}{2(L_d - L_q)} \pm \sqrt{\frac{\lambda_{mpm}^2}{4(L_d - L_q)^2} + i_q^2} \tag{5.20}$$

The first term of Equation 5.20 has a negative value since $L_q > L_d$. Hence, the positive sign for the second term is selected to minimize i_d. To implement the MTPA for the FMaSynRG, the reference values i_d^* and i_q^* are calculated according to Equation 5.22 and Equation 5.21. The schematic of the MTPA control is depicted in Figure 5.16.

$$i_q^* = \frac{2T_e^*}{3\mathfrak{p}(\lambda_{mpm} - (L_d - L_q)) i_d} \tag{5.21}$$

$$i_d^* = \frac{\lambda_{mpm}}{2(L_d - L_q)} + \sqrt{\frac{\lambda_{mpm}^2}{4(L_d - L_q)^2} + i_q^2} \tag{5.22}$$

5.4 Results

The results of the control system of the FMaSynRG are attained. Figure 5.17 illustrates the values of dq-axis currents to obtain the required torque. Consequently, the vq-axis voltages are also attained.

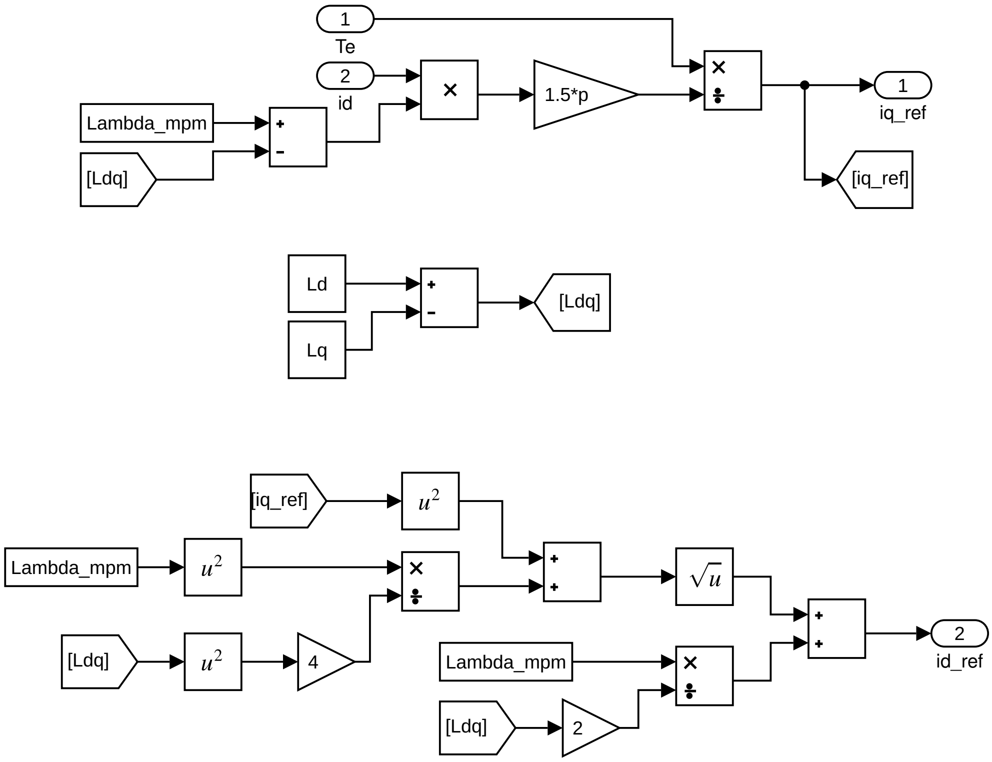

Figure 5.16: Block diagram of MTPA control

Then, the phase currents and voltages are found by means of frame transformation. Their respective waveforms are shown in Figure 5.18, where it can be seen that the shift angle between the phase current and voltage is around 22°, resulting in a power factor equal to 0.92. Moreover, the model is tested with two step inputs. Although there is an important peak voltage, the system reaches stability easily.

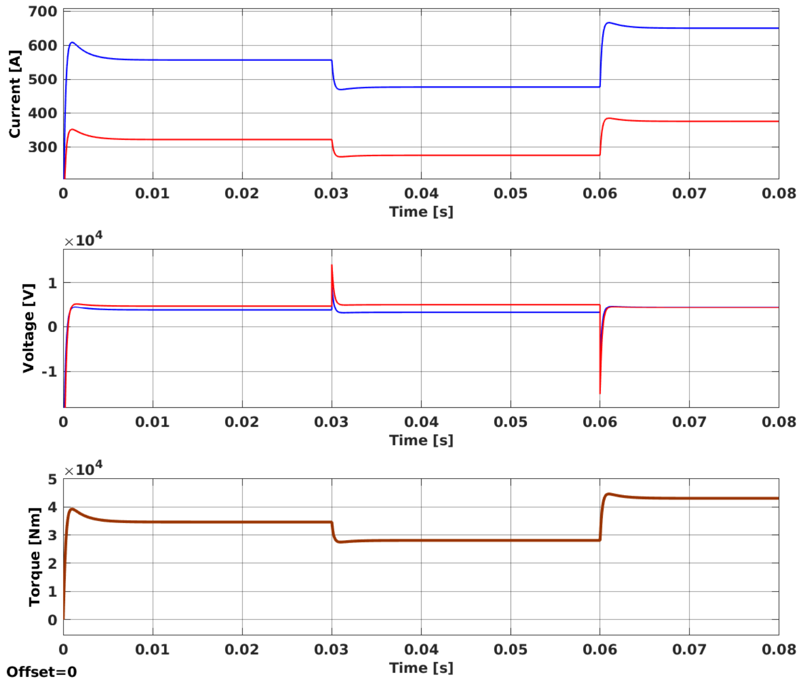

Figure 5.17: dq-axis currents, vq-axis voltages, and electromagnetic torque of FMaSynRG

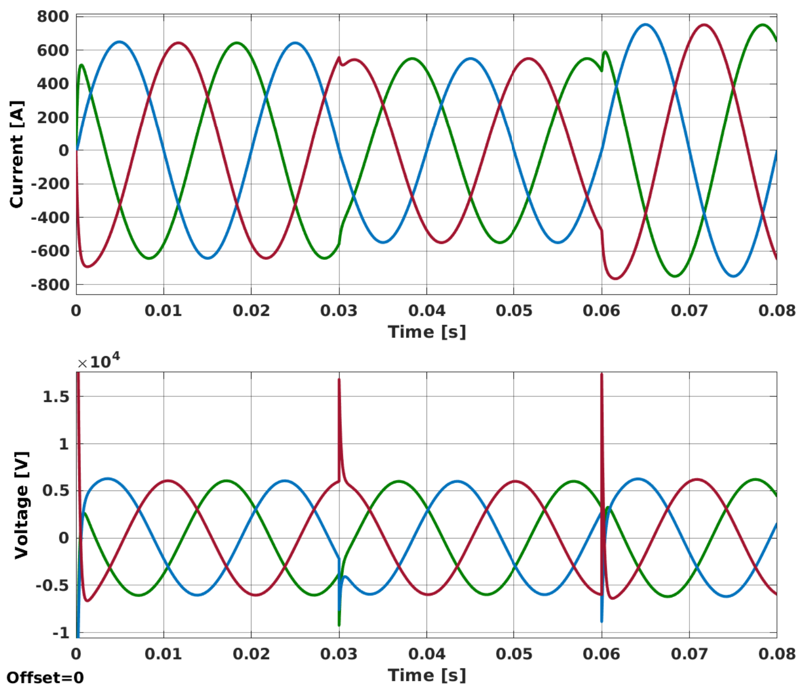

Figure 5.18: Phase currents and phase voltages

Chapter 6

Conclusions

In this report, a study design of a ferrite magnet-assisted synchronous reluctance generator for wind turbines was presented. The method to find the electromagnetic parameters based on finite element analysis was explained and compared with an existing machine, in order to ensure the accuracy of the outcomes. Also, two 5-MW generators were designed to understand the effects of some mechanical aspects on the machine performance. Moreover, the results of the designed FMaSynRG are contrasted with an IPMSG that has similar size. Finally, the maximum torque per ampere control strategy is employed in a wind power generation system, attaining good performance when the coupling back-EMF term is eliminated from the controller design. Concerning the above-mentioning work, the following main conclusions are drawn.

- The FMaSynRG was designed in such a way to be able to generate the same active power than the IPMSG of [10]. In both cases, the size of the machines are quite similar, with a small difference in their length (0.945 m for IPMSG and 0.989 m for FMaSynRG-R2). This is because the FMaSynRG uses more magnetic material, thence more flux density and electromagnetic torque generation. Also, an equivalent design (FMaSynRG-R1) with the same amount but different type of magnetic material than IPMSG was proposed. However, the ferrite magnet properties could not compete with the permanent magnets employed in the IPMSG. Additionally, the length of R1 was twice R2, thence FMaSynRG-R1 did not represent a good design approach.

- In a SynRM, the power factor is basically defined by the salient ratio, thence low value. Additionally, this salient ratio depends on the flux-barrier shape. By adding a magnetic material into the flux barriers, the rotor core is saturated and the increased back-EMF compensates the inductive effect in the machine, thus a better power factor is achieved. Therefore, a rotor structure with asymmetric flux barriers filled with permanent magnets is highly recommended, since it brings about a better power factor. Nevertheless, an important manufacturing issue that brings out is the appropriate Halbach ring to magnetize the 5-MW rotor.

- In general, the active total weight of the IPMSG is 6% higher than the designed FMaSynRG. Even though this represents saving material, it is not high enough to be considerable. However, if the stator of the IPMSG were kept in the FMaSynRG, the difference would lie on the rotor weight, on which the saving material only in the rotor core steel is about 40.6%. The comparable active weight of these two machines is because the stator windings have more number of conductors, so 29.7% more weight; and, the stator tooth is somewhat wider, then 4.5% more core steel.

- To design the control system, the FMaSynRG is treated as a PMSG since the same mathematical expression are utilized. Therefore, it is imperative to get rid of the coupling items, so that the plant becomes a stable first-order system. Even though no converter is connected or modelled, the control system contemplates the impact of a digital controller. In other words, both computational and PWM delays are taken into account. This not only helps to understand the real behavior of such systems, but also makes easier to find the gain of the PI controllers. As a result, the model can be extended to a complete circuit, where the back and front converters are necessary for power flowing to the grid.

6.1 Future Work

At the end of this project, the possibility to continue optimizing the structure and control system of FMaSynRG is opened. Since this project represented an introduction of how to design an electrical machine, some parameters and configurations remain outstanding.

- Increase the number of stator slots. Consequently, the winding factor is higher, thence a smoother flux waveform is obtained. However, the increased number of coils could raise the final cost, thus a trade-off study has to be contemplated.

- The rotor structure can also be optimized if the flux-barrier shape is replaced by a more asymmetric one. The actual flux barrier has some corners where the flux density is concentrated, then the losses are higher. Additionally, it was showed the effect that brings about the selection of an appropriate magnet coverage. However, with the proposed flux barrier and the amount of the needed magnetic material, was difficult to produced the required active power.

Bibliography

[1] Renewable Energy Policy Network for the 21st Centruey (REN21). Renewables 2017 global status report. www.ren21.net.

[2] M.P. Kazmierkowski. The electric generators handbook volume i: Synchronous generators and volume iiii: variable speed generators (boldea, i.; 2006) - [book review]. 1:41–41, 02 2007.

[3] J. K. Kostko. Polyphase reaction synchronous motors. *Journal of the American Institute of Electrical Engineers*, 42(11):1162–1168, Nov 1923.

[4] S. Tokunaga and K. Kesamaru. Fem simulation of novel small wind turbine generation system with synchronous reluctance generator. In *2011 International Conference on Electrical Machines and Systems*, pages 1–6, Aug 2011.

[5] A. J. Piña, H. Cai, Y. Alsmadi, and L. Xu. Analytical model for the minimization of torque ripple in permanent magnets assisted synchronous reluctance motors through asymmetric rotor poles. In *2015 IEEE Energy Conversion Congress and Exposition (ECCE)*, pages 5609–5615, Sept 2015.

[6] P. Roshanfekr, S. Lundmark, T. Thiringer, and M. Alatalo. A synchronous reluctance generator for a wind application-compared with an interior mounted permanent magnet synchronous generator. In *7th IET International Conference on Power Electronics, Machines and Drives (PEMD 2014)*, pages 1–5, April 2014.

[7] S. Nattuthurai and R. Neelamegham. Design and performance evaluation of synrm and ferrite assisted-synrm for ev application using fea. In *2017 International Conference On Smart Technologies For Smart Nation (SmartTechCon)*, pages 492–497, Aug 2017.

[8] Y. Hu, C. Liu, S. Zhu, and K. Wang. Optimized design of rotor structure in ferrite-assisted synchronous reluctance machines for electric vehicle application. In *2016 Eleventh International Conference on Ecological Vehicles and Renewable Energies (EVER)*, pages 1–7, April 2016.

[9] Wu Qian. *Moulding Technology based Ferrite Magnet assisted Synchronous Reluctance Machine.* Aalborg University, Aalborg, 2018.

[10] Poopak Roshanfekr. *Design and assessment of HVDC off-shore wind turbine generator.* Chalmers University of Technology, Göteborg, 2015. Diss. Göteborg : Chalmers tekniska högskola, 2015.

[11] Guru. B.S and Hiziroglu. Huseyin.R. *Electric Machinery and Transformers.* New York, 3rd edition edition.

[12] William H Hayt. *Engineering electromagnetics : 8th edition.* Mcgraw hill higher education, London, 8 ed. edition, 2012.

[13] Juha Pyrhonen. *Design of rotating electrical machines / Juha Pyrhönen, Tapani Jokinen, Valeria Hrabovcova.* Wiley, Chichester, elektronisk udgave. -second edition edition, 2014.

[14] Ramu Krishnan. *Permanent Magnet Synchronous and Brushless DC Motor Drives.* CRC Press, Hoboken, 2009.

[15] Fitzgerald. A.E and Jr. Kinsley. C. *Electric Machinery.* New Delhi, 6th edition edition.

[16] Oleg;Sudhoff Scott D.;Pekarek Steven Krause, Paul C.;Wasynczuk. *Analysis of Electric Machinery and Drive Systems.* Wiley-IEEE Press, 2013.

[17] K. Lu, P. O. Rasmussen, and E. Ritchie. A simple and general approach to determination of self and mutual inductances for ac machines. In *2011 International Conference on Electrical Machines and Systems*, pages 1–4, Aug 2011.

[18] G. De Donato, F. Giulii Capponi, G. A. Rivellini, and F. Caricchi. Integral-slot versus fractional-slot concentrated-winding axial-flux permanent-magnet machines: Comparative design, fea, and experimental tests. *IEEE Transactions on Industry Applications*, 48(5):1487–1495, Sept 2012.

[19] Q. Wu, K. Lu, P. O. Rasmussen, and K. F. Rasmussen. A new application and experimental validation of moulding technology for ferrite magnet assisted synchronous reluctance machine. In *2016 IEEE Energy Conversion Congress and Exposition (ECCE)*, pages 1–8, Sept 2016.

[20] E. Howard, M. J. Kamper, and S. Gerber. Asymmetric flux barrier and skew design optimization of reluctance synchronous machines. *IEEE Transactions on Industry Applications*, 51(5):3751–3760, Sept 2015.

[21] P. J. Lawrenson and L. A. Agu. Low-inertia reluctance machines. *Electrical Engineers, Proceedings of the Institution of*, 111(12):2017–2025, December 1964.

[22] V. B. Honsinger. Steady-state performance of reluctance machines. *IEEE Transactions on Power Apparatus and Systems*, PAS-90(1):305–317, Jan 1971.

[23] P. J. Lawrenson and L. A. Agu. Theory and performance of polyphase reluctance machines. *Electrical Engineers, Proceedings of the Institution of*, 111(8):1435–1445, August 1964.

[24] P. Niazi. *Permanent Magnet Assisted Synchronous Reluctance Motor, Design and Performance Improvement.* Texas A&M University, 2006.

[25] Carlos Enrique Imbaquingo Muñoz, Jesús Letosa Fleta, and Antonio Usón Sardaña. Análisis paramétrico mediante el método de elementos finitos en dos dimensiones de una máquina síncrona de excitación híbrida. 2013.

[26] D. Meeker, N. Bianchi, J. Gyselinck, R. V. Sabariego, L. Alberti, G. Pellegrino, and F. Cupertino. Electrical machine analysis using free software. In *2017 IEEE Energy Conversion Congress and Exposition (ECCE)*, pages 1–289, Oct 2017.

[27] Siegfried Heier. *Grid Integration of Wind Energy Conversion Systems.* John Wiley Sons Ltd, 1998.

[28] K. Sakata, H. Fujimoto, L. Peretti, and M. Zigliotto. Enhanced speed and current control of pmsm drives by perfect tracking algorithms. In *The 2010 International Power Electronics Conference - ECCE ASIA -*, pages 587–592, June 2010.

[29] D. G. Holmes, T. A. Lipo, B. P. McGrath, and W. Y. Kong. Optimized design of stationary frame three phase ac current regulators. *IEEE Transactions on Power Electronics*, 24(11):2417–2426, Nov 2009.

[30] A. Purwadi, R. Hutahaean, A. Rizqiawan, N. Heryana, N. A. Heryanto, and H. Hindersah. Comparison of maximum torque per ampere and constant torque angle control for 30kw interior interior permanent magnet synchronous motor. In *Proceedings of the Joint International Conference on Electric Vehicular Technology and Industrial, Mechanical, Electrical and Chemical Engineering (ICEVT IMECE)*, pages 253–257, Nov 2015.

[31] Reza Rajabi Moghaddam. *Synchronous Reluctance Machine (SynRM) in Variable Speed Drives (VSD) Applications.* PhD thesis, KTH, Electrical Machines and Power Electronics (closed 20110930), 2011. QC 20110518.

[32] Yongqiang; Zargari Navid; Kouro Samir Wu, Bin; Lang and Yongqiang Lang. *IEEE Press Series on Power Engineering : Power Conversion and Control of Wind Energy Systems.* 2011.

Appendix A

Magnetic Properties

Table A.1 details the points of the BH-curve of the different materials utilized in this project.
Table A.2 lists the equivalent core loss per kg with respect the frequency and the magnetic flux density. Density for M270-35A is 7.65 kg/dm^3.

M270-35A		Ferrite Magnet		Halbach Magnet		Shaft	
B [T]	**H** [A/m]	**B** [T]	**H** [A/m]	**B** [T]	**H** [A/m]	**B** [T]	**H** [A/m]
0.00	0.00	0.000	-192000	0.000	-950000	0.0000	0.0000
0.10	30.0	0.0068	-191841	0.0323	-925600	0.00483	0.1000
0.20	39.6	0.0136	-189000	0.0646	-901300	0.0641	132.7394
0.30	46.0	0.0205	-186000	0.0969	-876900	0.1281	265.3788
0.40	52.0	0.0273	-181000	0.1292	-852600	0.1921	398.0182
0.50	58.2	0.0341	-176000	0.1615	-828200	0.2561	530.6576
0.60	65.2	0.0409	-171000	0.1938	-803800	0.3201	663.2971
0.70	73.3	0.0477	-165000	0.2262	-779500	0.3841	795.9365
0.80	83.1	0.0546	-160000	0.2585	-755100	0.4481	928.5759
0.90	95.5	0.0614	-155000	0.2908	-730800	0.5121	1061.215
1.00	112	0.0682	-150000	0.3231	-706400	0.5761	1193.855
1.10	136	0.0750	-145000	0.3554	-682100	0.5762	2387.909
1.20	178	0.0818	-140000	0.3877	-657700	1.0681	2387.909
1.30	272	0.0887	-134000	0.4200	-633300	1.3564	3581.864
1.40	596	0.0955	-129000	0.4523	-609000	1.5278	4775.819
1.50	1700	0.1023	-124000	0.4846	-584600	1.6321	5969.773
1.60	3880	0.1091	-119000	0.5169	-560300	1.6988	7163.728
1.70	7160	0.1159	-114000	0.5492	-535900	1.7455	8357.683
1.80	11600	0.1228	-109000	0.5815	-511500	1.7814	9551.638
		0.1296	-103000	0.6138	-487200	1.8108	10745.59
		0.1364	-98200	0.6462	-462800	1.8360	11939.55
		0.1432	-93000	0.6785	-438500	1.8581	13133.5
		0.1501	-87900	0.7108	-414100	1.8779	14327.46
		0.1569	-82700	0.7431	-389700	1.8959	15521.41
		0.1637	-77500	0.7754	-365400	1.9122	16715.37
		0.1705	-72400	0.8077	-341000	1.9273	17909.32
		0.1773	-67200	0.8400	-316700	1.9411	19103.28
		0.1842	-62000	0.8723	-292300	1.9539	20297.23
		0.1910	-56900	0.9046	-267900	1.9658	21491.18
		0.1978	-51700	0.9369	-243600	1.9768	22685.14
		0.2046	-46500	0.9692	-219200	1.9871	23879.09
		0.2114	-41400	1.0015	-194900	1.9966	25073.05
		0.2183	-36200	1.0338	-170500	2.0054	26267.00
		0.2251	-31000	1.0662	-146200	2.0136	27460.96
		0.2319	-25900	1.0985	-121800	2.0212	28654.91
		0.2387	-20700	1.1308	-97440	2.0283	29848.87
		0.2455	-15500	1.1631	-73080	2.0349	31042.82
		0.2524	-10300	1.1954	-48720	2.0410	32236.78
		0.2592	-5169	1.2277	-24360	2.0467	33430.73
		0.266	0	1.2600	0.0000	2.0520	34624.69
						2.0569	35818.64
						2.0615	37012.60
						2.0659	38206.55
						2.0699	39400.50
						2.0738	40594.46
						2.0774	41788.41
						2.0808	42982.37
						2.0841	44176.32
						2.0872	45370.28
						2.0902	46564.23

Table A.1: Peak magnetic field strength and peak flux density

50 Hz		60 Hz		100 Hz		200 Hz		400 Hz	
[T]	[W/kg]	[T]	[W/kg]	[T]	[W/kg]	[T]	[W/kg]	[T]	[W/kg]
0.05	0.00304	0.04997	0.00371	0.05	0.00701	0.05	0.01721	0.04991	0.0492
0.1	0.01475	0.09995	0.01826	0.10001	0.03382	0.09992	0.08041	0.09998	0.21873
0.14995	0.03534	0.15	0.04374	0.15004	0.08055	0.15001	0.1908	0.14998	0.50711
0.20002	0.063	0.19996	0.07801	0.19998	0.14355	0.20002	0.34094	0.20001	0.89945
0.25002	0.09644	0.25002	0.11924	0.24997	0.21996	0.24993	0.52467	0.25003	1.3807
0.29996	0.13437	0.29972	0.16611	0.2999	0.30753	0.29975	0.73729	0.30009	1.9179
0.34996	0.17631	0.34993	0.21835	0.35001	0.40537	0.35004	0.96998	0.3497	2.5391
0.39995	0.22182	0.40006	0.27514	0.39974	0.51149	0.39981	1.2316	0.39989	3.2509
0.45007	0.27077	0.44979	0.33559	0.44982	0.62644	0.4498	1.5168	0.44984	4.0111
0.50001	0.3227	0.49992	0.40021	0.5	0.74989	0.49996	1.8249	0.4999	4.843
0.55004	0.37761	0.55005	0.46887	0.55013	0.88059	0.54994	2.152	0.54985	5.7326
0.6001	0.435	0.59981	0.5405	0.59982	1.0174	0.59987	2.4997	0.5998	6.6886
0.65014	0.49524	0.64995	0.61574	0.64999	1.1626	0.64987	2.8713	0.64984	7.7122
0.69979	0.55771	0.70016	0.6945	0.70012	1.3147	0.69983	3.2613	0.69977	8.8057
0.74986	0.62327	0.74991	0.77611	0.74979	1.4723	0.74977	3.6817	0.74993	9.9693
0.80002	0.69164	0.80003	0.86195	0.79991	1.6391	0.79992	4.118	0.79997	11.211
0.84982	0.76286	0.84967	0.95106	0.84997	1.812	0.84988	4.5742	0.84962	12.527
0.90027	0.83816	0.90015	1.0454	0.89966	1.9918	0.89969	5.0521	0.8996	13.93
0.94989	0.91586	0.94972	1.1424	0.94995	2.183	0.94964	5.5549	0.94989	15.434
0.99996	0.99824	0.99981	1.2456	0.99996	2.3827	0.99953	6.0825	0.9997	17.013
1.05	1.0851	1.0498	1.3544	1.05	2.5928	1.0497	6.6452	1.05	18.705
1.1001	1.1775	1.0999	1.4699	1.0999	2.8152	1.0996	7.2334	1.0997	20.475
1.1503	1.2762	1.1501	1.5932	1.1499	3.0531	1.1497	7.8696	1.15	22.385
1.2001	1.3828	1.2003	1.7276	1.2	3.3106	1.1998	8.5435	1.2	24.39
1.2503	1.5004	1.2504	1.8735	1.2501	3.5911	1.2498	9.2669	1.2499	26.517
1.3	1.6289	1.3	2.0339	1.2999	3.8996	1.2999	10.063	1.2998	28.818
1.3503	1.7762	1.3501	2.2172	1.3503	4.2507	1.3501	10.964	1.3502	31.388
1.4002	1.9366	1.4008	2.4219	1.4003	4.6234	1.4003	11.968	1.4004	34.262
1.4506	2.1214	1.4509	2.652	1.4508	5.0655	1.4506	13.137	1.4505	37.486
1.5011	2.3138	1.5014	2.8783	1.5011	5.5137	1.5012	14.364	1.5014	40.979
1.5522	2.4875	1.5525	3.1147	1.5524	5.9367	1.5521	15.634	1.5522	44.947
1.6034	2.6471	1.6036	3.3158	1.6038	6.3255	1.604	16.93	1.6036	49.017
1.6554	2.782	1.6553	3.5055	1.6554	6.7329	1.6548	18.273	1.655	53.155
1.708	2.957	1.7078	3.6667	1.7079	7.0777	1.6561	18.365	1.6577	53.347
1.7604	3.0826	1.7602	3.8119	1.7604	7.4096				
1.8134	3.2188	1.8133	3.9672	1.8138	7.6737				
1.8677	3.2981	1.8675	4.0847	1.8677	7.9388				
1.9236	3.3909	1.9237	4.1863						

Table A.2: Core losses for lamination M270-35A

Appendix B

Power Factor as a Function of Salient Ratio

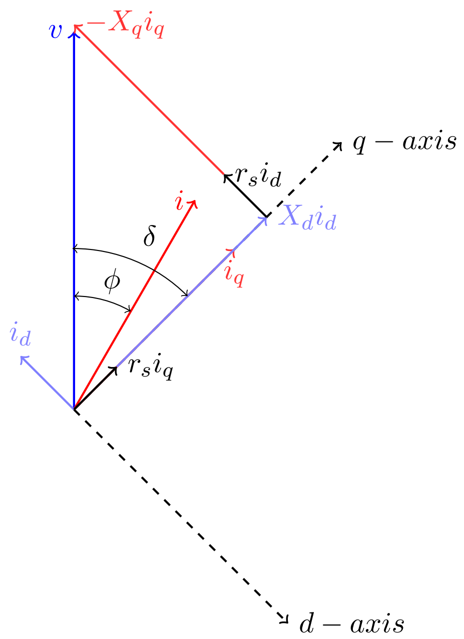

Figure B.1: Phasor diagram of SynRM

$$v_q = r_s i_q + \omega\lambda_d + p(\lambda_q) \tag{B.1}$$
$$v_d = r_s i_d - \omega\lambda_q + p(\lambda_d) \tag{B.2}$$

where:

$$\lambda_q = L_q i_q \tag{B.3}$$
$$\lambda_d = L_d i_d + \lambda_{mpm} \tag{B.4}$$

In SynRM the the magnet peak value λ_{mpm} is equal to zero, and the inductances L_d and L_q are approximately constant, then

$$v_q = r_s i_q + \omega\lambda_d = r_s i_q + X_d i_d \tag{B.5}$$
$$v_d = r_s i_d - \omega\lambda_q = r_s i_d + X_q i_q \tag{B.6}$$

Also, from Figure B.1 it can be see that

$$V cos(\delta) = r_s i_q + x_d i_d \tag{B.7}$$
$$V sin(\delta) = r_s i_d + X_q i_q \tag{B.8}$$

By replacing Equation B.7 and Equation B.8 into Equation B.6, the currents in the d- and q-axis are

$$i_d = \frac{V(r_s sin(\delta) + X_q cos(\delta))}{r_s^2 + X_d X_q} \tag{B.9}$$
$$i_q = \frac{V(r_s cos(\delta) - X_d sin(\delta))}{r_s^2 + X_d X_q} \tag{B.10}$$

Furthermore, the active and reactive power are found by projecting the currents i_d and i_q along the voltage axes.

$$P_i = mV(i_q cos(\delta) + i_d sin(\delta)) \tag{B.11}$$
$$Q_i = mV(i_q sin(\delta) - i_d cos(\delta)) \tag{B.12}$$

where m is the number of phases. Thus, the apparent power can be represented as

$$S_i = \sqrt{P_i^2 + Q_i^2} = mV\sqrt{i_q^2 + i_d^2} \tag{B.13}$$

By definition the power factor is the ration between the active and apparent power, as a result

$$cos(\phi) = \frac{i_q cos(\delta) + i_d sin(\delta)}{\sqrt{i_q^2 + i_d^2}} \tag{B.14}$$

If the pessimistic case is assumed r_s=0. Even though it is clear that any resistive component will raise the power factor, so:

$$i_d = \frac{V}{X_d} cos(\delta) \tag{B.15}$$

$$i_q = -\frac{V}{X_q} sin(\delta) \tag{B.16}$$

Now, Equation B.15 and Equation B.16 are replaced into Equation B.14. After some mathematical procedure, the power factor can be found as a function of the inductances and MMF angle δ,

$$cos(\phi) = \frac{L_q - L_d}{\sqrt{\frac{L_d^2}{cos^2(\delta)} + \frac{L_q^2}{sin^2(\delta)}}} \tag{B.17}$$

To simplify the analysis, two constants are used to identify the salient ratio and the MMF angle δ as it follows,

$$k = \frac{L_q}{L_d} \tag{B.18}$$

$$x = sin^2(\delta) \tag{B.19}$$

then

$$cos(\phi) = \frac{k-1}{\sqrt{\frac{k^2}{x} + \frac{1}{1-x}}} \tag{B.20}$$

In order to find the maximum value of $cos(\delta)$, the derivative of Equation B.20 with respect to x is equal to zero,

$$\frac{d}{dx} cos(\phi) = (k-1)\left(\frac{k^2}{x} + \frac{1}{1-x}\right)^{-3/2}\left(-\frac{k^2}{x^2} + \frac{1}{(1-x)^2}\right) = 0 \tag{B.21}$$

The first term of Equation B.21 has no possible solution, hence only the second term is evaluated as is depicted below,

$$-\frac{k^2}{x^2} + \frac{1}{(1-x)^2} = 0$$

$$x = k(1-x)$$

$$sin^2(\delta) = k\, cos^2(\delta)$$

$$tan(\delta) = \sqrt{k} \tag{B.22}$$

Additionally, some trigonometric identities are used

$$sin^2(\delta) = \frac{tan^2(\delta)}{1 + tan^2(\delta)} \tag{B.23}$$

$$cos^2(\delta) = 1 - \frac{tan^2(\delta)}{1 + tan^2(\delta)} \tag{B.24}$$

Finally, Equation B.22, Equation B.23 and Equation B.24 are substituted into Equation B.20, where the maximum power factor is found as a function of the salient ratio.

$$cos(\phi)_{max} = \frac{k-1}{k+1} = \frac{L_q - L_d}{L_q + L_d} \tag{B.25}$$

Appendix C

Calculation of Power Factor

The back-EMF is calculated without considering the drop voltages, so the equivalent equations are:

$$e_d = -\omega_r \lambda_q \tag{C.1}$$
$$e_q = \omega_r \lambda_d \tag{C.2}$$

By replacing the data from Table 4.9,

$$e_d = -(100\pi)(-21.86) = 2186\pi$$
$$e_q = (100\pi)(-2.84) = -284\pi$$

Then, the terminal voltages are found taking as a reference the circuits in Figure C.1 and Figure C.2.

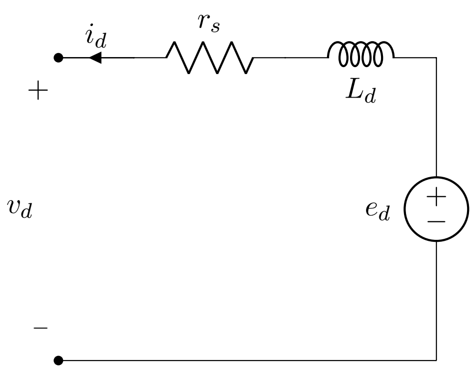

Figure C.1: Simplified d-axis circuit

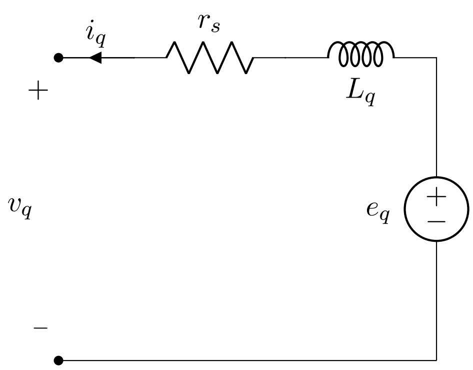

Figure C.2: Simplified q-axis circuit

$$u_d = e_d - r_s i_d - jX_d i_d \tag{C.3}$$
$$u_q = e_q - r_s i_q - jX_q i_q \tag{C.4}$$

Next, the given data is substituted

$$
\begin{aligned}
e_{dq} &= 2186\pi - j284\pi \\
i_{dq} &= 556.8 + j312.45 \\
r_s &= 0.03991 \\
L_{dq} &= 0.01257 + j0.03752
\end{aligned}
$$

$$
\begin{aligned}
u_{dq} &= e_{dq} - r_s i_{dq} - L_{dq} i_{dq} \\
&= 6850 - j929.5 \\
&= 6912.8 \quad \angle -7.7^{\circ}
\end{aligned}
$$

$$i_{dq} = 642.9 \quad \angle 30^{\circ}$$

Then the power factor,

$$cos(\phi) = cos(\phi_v - \phi_i) = cos(-37.7) = 0.79$$